Inorganic light absorbers for printable solar cell applications

GRADUATE SCHOOL OF LIFE SCIENCE AND SYSTEM ENGINEERING

KYUSHU INSTITUTE OF TECHNOLOGY

DISSERTATION

FOR THE DEGREE OF

DOCTOR OF PHILOSOPHY

Murugan Vigneshwaran

SUPERVISOR

Professor. Shuzi Hayase

DIVISION OF GREEN ELECTRONICS

GRADUATE SCHOOL OF LIFE SCIENCE AND SYSTEMS ENGINEERING

KYUSHU INSTITUTE OF TECHNOLOGY

Abstract

$MAPbI_3$ with chloride additive is the suitable material for planar architecture of perovskite solar cells and it also have very good photoluminescence property. Addition of chloride ions highly enhances the carrier life time, diffusion length, crystal formation and film morphology in $MAPbI_3$. Different chloride based additives are highly crucial in deciding most of the physicochemical properties in lead based perovskite $CH_3NH_3PbI_3$. In the present study optimized quantity and nature of chloride precursor used for formation of large perovskite crystals with minimal disorder were explored. It was found that the addition of ethyl ammonium chloride (EACl) increased the crystal size, which is nearly twice (158 nm) the size of standard perovskite crystals (93 nm) having a preferential orientation towards the (110) plane. Photoacoustic studies demonstrated that the disorder in the perovskite crystals was highly reduced by the addition of the EACl precursor. The effect of the alkyl chain length of an alkyl ammonium chloride precursor on the crystal growth of $CH_3NH_3PbI_3$ was systematically investigated. In addition, we also used the different solvents in two step method with EACl to reduce the surface roughness of the perovskite layer.

Recently, bismuth based perovskites with the structure $(CH_3NH_3)_3Bi_2I_9$ (MBI) are rapidly emerging as eco-friendly and stable semiconducting material as a substitute for the lead halide perovskites. Relatively wider bandgap of MBI (~ 2.1 eV) has been found to be a bottleneck in realizing the high photovoltaic performance similar to that of lead halide based perovskites. Therefore, we demonstrated the bandgap engineering of novel bismuth based perovskites obtained by in-situ sulfur doping of MBI via the thermal decomposition of $Bi(xt)_3$ (xt = Ethyl Xanthate) precursor. Color of the obtained films were clearly changed from orange to black when annealed from 80^oC to 120^oC with bandgap of 1.45 eV, which is even lower than that of most commonly used lead halide perovskites. After successfully reduced the bandgap of the materials, the electronic properties of the material was also studied to find its suitability in the solar cells. The electronic properties such as carrier concentration, mobility, and carrier life time was found to be higher in sulfur doped MBI when compared to undoped MBI.

Table of contents

Chapter 1. Introduction

1.1 Renewable energy

Most of the developed nations relies on the non-renewable energy sources like coal, oil, and natural gas for its energy. Usage of fossil fuels are very hazardous to the nature due to the emission of carbon dioxide, nitrogen dioxide, sulfur dioxide, carbon monoxide etc. Which are responsible for the air pollution also non-renewable resources will be less in supply in the future. So, extraction of power from renewable energy that are continuously restored by nature like the sun, the wind, water, the Earth's heat, and plants are necessary. Technologies which are employed to convert this renewable fuels to energy should be developed in the large scale. These are named as "clean" or "green" technologies since they produce very negligible amount of pollutants to the atmosphere [1]. There are many types of technologies to convert these natural energy resources which could be explained in brief. Figure 1 shows the different kinds of renewable energy sources available globally. Organic matter which is obtained from the living organisms like plants or dung from animals can be termed as the biomass. Through combustion of these organic matters energy can be produced by heat also by converting it into biofuels. Generally thermal, chemical, and biochemical are the methods used to convert biomass to bio fuels. However, recent studies

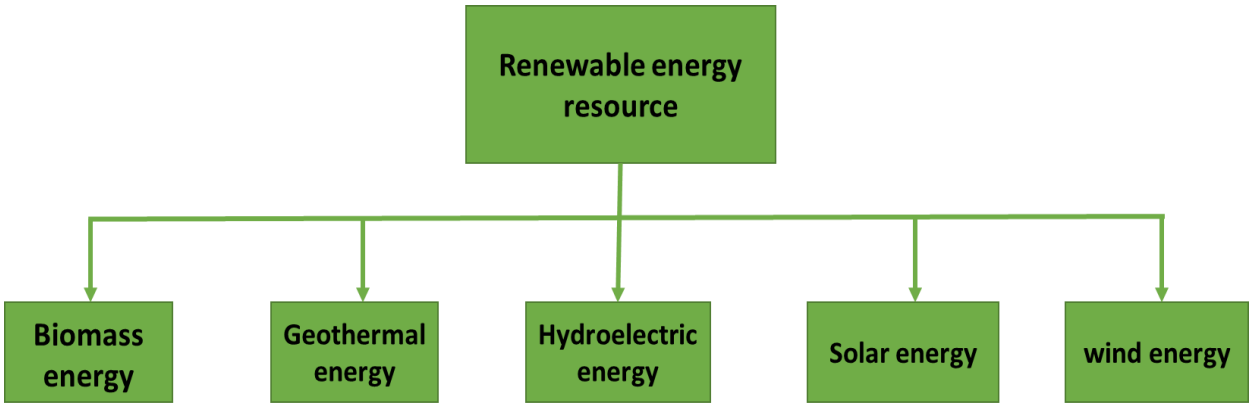

Figure. 1 Different kinds of renewable energy sources

show little to no economic potential to increase bio power in the U.S. over the next two decades because of its relatively high costs compared with other renewable energy and low carbon technologies [2]. Power can be generated through wind a kind of solar energy. Uneven heating of the atmosphere by the sun, the irregularities of the earth's surface, and rotation of the earth are the

primary cause for the generation of wind. Wind turbines are used to harvest the motion energy to generate power [3]. The main demerit in using wind energy are cost issues, environmental concerns like noise pollution, aesthetic impacts, and supply and transport issues.

Using the thermal energy obtained from the earth crust geothermal energy is generated. Hot water or steam reservoirs that are accessed by drilling deep in to the earth thermal energy can be obtained. Hydrogen is the power source in fuel cells when hydrogen is consumed it produces only water, a clean fuel for the future. The general sources for hydrogen are natural gas, nuclear power, biomass, and renewable power like solar and wind. The good options with hydrogen energy is it can be used to store, move, and deliver energy produced from other sources. Natural gas reforming and electrolysis are the major conventional methods used for producing hydrogen fuel [4].

Another important renewable power source is ocean energy which can be classified into two types i) thermal energy from the sun's heat, and ii) mechanical energy from the tides and waves. They are the world's biggest solar collectors since oceans occupy 70% of Earth's surface. Surface of sea water is heated more when compared to the deep shallow water and this difference in temperature creates thermal energy. Heat trapped in small range in oceans are much enough to power the world. Closed-cycle, open-cycle, and hybrid are the three types of systems used in electricity conversion of ocean energy [5].

Hydropower is the endless energy source obtained from the kinetic energy of falling and fast running water. It costs less than most of the energy sources. Through the pipe generally called penstock the fast running water will be transferred which in turn causes the blades in turbine to rotate and hence the power generates [4]. The amount of sunlight that hits the earth`s surface for 90 minutes can contribute electricity to the whole world for the entire year. So, among all kind of renewable energy sources solar energy are very crucial and also the topic of our interest which needs elaborate discussion.

1.2 Importance of solar energy

Compared to other renewable energy sources. Even though solar energy has the greater potential at present it just only covers 0.05% of the total global energy demands (1% of total electricity supply). The major reason for less utilization of solar energy is due to its high cost when compared to other renewable energy sources. But solar energy is the best option for decentralized

energy supply in the remote regions of the earth [6], [7]. Total cumulative solar energy installed worldwide is 22928.9 MW in 2009 from BP statistical energy survey [8].

The expected future of solar energy technology at 2005 is 15 GW in 2010 versus 2.7 GW in 2006. Successful growth of silicon solar cells was also proved by 41,000 tons in 2006 to 120,000 tons in 2010 and 400,000 tons in 2015. The upcoming development and installation of electricity through solar cells are highly motivated in developed nations like USA, Europe, and Japan [9].

The major advantages of solar energy is i) No greenhouse or toxic gas emission ii) Degraded lands will be recovered iii) Quality of water resources will be improved iv) Very important in supplying electricity to rural areas in developing countries. Also solar energy is very reliable unlike wind energy it is very consistent.

Utilization of solar energy is mandatory in order to make the financial cost of the electricity lower, since no cost for sunlight and fabricating solar cells doesn't need any mining or fuel processing. Solar panels can also be used as the additional power source to reduce the total cost provided for the electricity. Nuclear energy is also the best candidate in the production of very clean or green energy with less cost also without causing any air pollution even though it creates lots of harmful wastes to the sea water. Catastrophic events like chernobyl meltdown is possible due to the long lasting of nuclear wastages in the reactors.

1.3 Different types of solar energy absorbers

1.3.1 Inorganic absorbers

Crystalline, multicrystalline, amorphous, and microcrystalline Si, the III-V compounds and alloys, CdTe, and the chalcopyrite compound, copper indium gallium diselenide (CIGS) are the major inorganic materials utilized for photovoltaic application. In crystalline Si devices, using the Czochralski method a boule of B-doped *p*-type Si is grown [10]. Crystalline silicon materials has the very low optical absorption coefficient due to its indirect bandgap. So, the silicon wafer should be 200 μm thick in order to increase the absorption of incident light. For multicrystalline solar cells Si ingots with large columnar grains about 0.3 mm in diameter is obtained by pouring molten Si into a container followed cooling process [11]. Passivation of grain boundaries plays the crucial

role which is done by incorporating hydrogen into the device. Since hydrogen is used in this process silicon nitride is used as the top insulating layer when compared to SiO_2 through plasma-enhanced chemical vapor deposition (PECVD). PECVD with silane (SiH_4) is the conventional technique used for growing amorphous Si thin films [12]. For continuous production and diversity of use amorphous silicon layers can be grown rigid substrates and also flexible substrates. In the passivation of dangling bonds hydrogen plays the unique role which is generally the alloy of Si and hydrogen.

Direct energy bandgaps, high optical absorption coefficients, with good values of minority carrier lifetimes and mobilities are the major merits in III-V compounds, such as GaAs, InP, and GaSb [13]. Due to the narrow bandgap of the GaAs and InP around 1.4 eV they are mostly employed as the single-junction solar cells. Manufacturing highly expensive device-quality substrates or epitaxial layers of these compounds is the main drawback for III-V compounds solar cells. Low cost deposition methods cannot be employed since crystal imperfections also other unwanted impurities strongly affects the device performance. They also have lower mechanical strength comparatively with silicon materials.

In thin film solar cells few microns of CdTe are needed to absorb most of the incident light due to the high optical absorption coefficient and direct bandgap of 1.5 eV. In this case material costs are highly minimized since thin layer is enough with short minority diffusion length costly processing is avoidable. $CuInSe_2$ (CIS) was the first chalcopyrite solar cells developed with narrow bandgap. After crucial finding in widening the energy bandgap to 1.3 eV by incorporating Ga with improved material quality made it the potential candidate for the solar cells with high efficiencies. Similar to CdTe based thin film solar cells photon absorption is too high due to the high optical absorption coefficient and needs few micron thickness to capture incident light which reducing the fabrication cost [14].

1.3.2 Organic absorbers

Tang et al and Albrecht et al in 1975 found that the organic materials has the potential for photovoltaic application but the efficiency was very low (Schottky diode solar cell with chlorophyll-a). First progress was made in 1986 by Tang with device architecture of copper phthalocyanine (CuPc) as the donor layer and 3,4,9,10-perylenetetracarboxylic-bis-benzimidazole

(PTCBI) as the acceptor layer and achieved 1% efficiency. Small molecules like 5,5-bis{(4-(7-hexylthiophen-2-yl)thiophen-2-yl)-[1,2,5]thiadiazolo[3,4-c]pyridine}-3,3-di-2ethylhexylsilylene-2,2-bithiophene as the donor and DTS($PTTh_2$)$_2$ with $PC_{70}BM$ as an acceptor were used to make bulk heterojunction device and efficiency of 6.7 % was achieved in 2012.

In case of polymer solar cells Heeger et al, Shirakawa et al, and Mac et al found an unique properties of organic conducting polymers on polyacetylene at 1970. The intrinsic conductive properties of these highly conjugated materials is mainly due to the sp^2 hybridized bonds with the unhybridized bond. Polymer solar cells are preferable when compared to the small molecule solar cells due to the phase separation in the same solvent and fast exciton dissociation. PCBM and P3HT are the most widely used polymers in OPVs. Tandem Organic Solar Cells was also worth mentioning since polymer solar cells has selective coverage in the solar spectrum.

Incorporation of carbon nanotubes (CNT) with polymer nanocomposites is another important aspect in the field of photovoltaics. CNT can be used as the transparent conductive layer for replacing ITO also as the composite with conducting polymers. Similarly materials like graphene, also CNT with polymer bulk heterojunction made a remarkable plots in the field of organic solar cells [16]. Table 1 shows the confirmed efficiency obtained for different kinds of solar cells under the global AM1.5 spectrum.

1.3.3 Sensitized dye as absorbers

A dye-sensitized solar cells generally consist of transparent conducting oxide electrode above that dye sensitized titanium dioxide nanoparticles film, with a platinum electrode and an electrolyte generally containing iodide [17].

Porphyrins dye structure attracted the attention due to the similarity with natural photosynthetic processes, also phthalocyanine dye structures for their photochemical and phototherapeutic applications. Even though while comparing to N3 or black dye sensitizer they are not good players in DSC because of their incapability to near IR region in the spectrum. So, idea for covering the broad spectrum is by mixing two dyes at visible and near IR region to make the cocktail. Generally the preferred combination is porphyrines and phthalocyanines which is applied to mesoporous TiO_2 as the mixture.

Table 1. Confirmed efficiency obtained for different kinds of solar cells under the global AM1.5 spectrum. [15]

Classification	Efficiency (%)	Area (cm^2)	Voc (V)	Jsc (mA/cm^2)	Fill factor (%)
Silicon (crystalline)	25.6 ± 0.5	143.7 (da)	0.740	41.8	82.7
Silicon (polycrystalline)	20.8 ± 0.6	243.9	0.6626	39.03	80.3
Si (thin transfer submodule)	21.2 ± 0.4	239.7	0.687	38.50	80.3
GaAs (thin film)	8.8 ± 0.9	0.9927	1.122	29.6	86.5
GaAs (polycrystalline)	18.4 ± 0.5	4.011	0.994	23.2	79.7
InP (crystalline)	22.1 ± 0.7	4.02	0.878	29.5	85.4
CIGS (cell)	20.5 ± 0.6	0.9882	0.752	35.3	77.2
Si (amorphous)	10.2 ± 0.3	1.001	0.896	16.36	69.8
Dye sensitized	11.9 ± 0.4	1.005	0.744	22.47	71.2
Organic thin-film	11.0 ± 0.3	0.993	0.793	19.40	71.4
InGaP/GaAs/InGaAs	37.9 ± 1.2	1.047	3.065	14.27	86.7

In panchromatic sensitizers application of semiconductor quantum dots are remarkable. The compounds in II–VI and III–V groups at below 5 nm can yield the desired quantum confinement effect. By utilizing this property the absorption spectrum of the can be modified by changing the size of the quantum dots. For single junction solar spectrum materials like InAs and PbS are used with the tuned bandgap of 1.35 eV [18].

1.4 Importance of perovskite material as light absorbers

1.4.1 Perovskite materials

In 1978, weber reported the structure and physical properties of organometal halide perovskites $CH_3NH_3MX_3$ (M = Pb or Sn, X = Cl, Br or I) which is now reaching high success in the field of solar cells. At ambient temperature Pb- and Sn- based halide perovskite materials were stabilized normally in the cubic perovskite structure. In these kind of structures the unit cell parameters depends on the size of the halides X = Cl, Br or I and it lies between 5.68 to 6.27 Å. The lattice parameters can also be tuned using the mixed halides [19]. The first unique property which made the scientific community to turn back toward the perovskite is by increasing the number of inorganic layers in the $(C_4H_9NH_3)_2$ $(CH_3NH_3)_{n-1}SnI_{3n+1}$ the material can be tuned from insulator to metal. However most of the researchers focused to use this material as the superconductors and very less attention was paid for the photovoltaic applications until 2009.

Phase transitions with temperature in methyl ammonium (MA = $CH_3NH_3^+$) based halide perovskite is the interesting point to note because of the molecular motion of methyl ammonium cation. Using NMR spectra degree of rotation was investigated in which rapid rotation was observed at high temperature and at low temperature it was restricted.

For the $CH_3NH_3PbI_3$ nanodots coated on the nanocrystalline thin film TiO_2 absorption co-efficient was estimated to be 1.5×10^4 cm $^{-1}$ at 550 nm, this clearly indicates the diffusion length as 0.66 μm. From photoluminescence spectroscopy the PL values for $CH_3NH_3PbI_3$ was found to be 750 nm and for $HC(NH_2)_2PbI_3$ as 850 nm. But in the case of $CH_3NH_3SnI_3$ red shift around 180 nm was determined in comparison with conventional lead halide perovskites.

Diffusion length is the very important parameter in fixing the performance of the perovskite solar cells. Thicker absorber layer with large diffusion length indicates the better light harvesting nature. Diffusion length of the solution gown single crystal reduces as the light intensity was increased. In the case of $CH_3NH_3PbI_{3-x}Cl_x$, 1 μm diffusion length for the electrons was reported. Even though after the serious research on perovskite solar cells the big question was either excitons

or free carriers are existing. Excitons are tightly bound while the free carriers are available at bottom and top electrode. Till now the binding energy of 19-15 meV was reported for lead based perovskites. Even in various measurements like optical absorption, magneto-absorption, and temperature-dependent photoluminescence (PL) the obtained exciton binding energy was of ~25 meV at room temperature.

DFT was used to study the physics behind the unusual defects in the perovskites. In lead based perovskites positively charged lead (Pb^{2+}) and methyl ammonium (MA^{+}) ions are responsible for defects with the lowest energy formation. These kind of defects are strongly depends on the preparation method. Lead based perovskites may be n-type or p-type depends on the ratio of precursors.

Although there is rapid development in perovskite field crystallinity and morphology control are the sections which deserves the high focus. Achieving uniform, quality crystals with 100% surface coverage pin hole free are highly needed realize good light harvesting, charge carrier transport and high diffusion length. Charge recombination mainly occur due to the grain boundary, and defect states in perovskite crystallites. Mesoporous perovskite films has the limitation to grow bigger crystal due to its pore size [45].

1.4.2 Different types of perovskite light absorbers

1.4.2.1 Halide Substitution in $MAPbX_3$

Substitution of different halide from Cl to Br shows the difference in the lattice constant, and increase in the bandgap from I to Br, and Cl. Increase in the electronegativity due to increase in covalent bonding nature of halogens with metal was found to be the major reason for the increase in bandgap. Using mixed halide perovskite like iodine with Br or Cl with Br the bandgap of the perovskites can be easily tuned in the complete visible spectra. Nevertheless, in the combination of iodine and Cl no shift in the bandgap was reported yet. This clearly shows that in PbI_6 octahedron Cl cannot replace the iodine [46].

Table 2. Comparison of charge transport bandgap (E_g) with optical band gap (E_{opt}) with exciton binding energy. [44]

Materials	E_g (eV)	E_{opt} (eV)	Δ (eV)
$MAPbI_3$	1.70 ± 0.10	1.52 ± 0.02	0.18 ± 0.10
$MAPbBr_3$	2.32 ± 0.10	1.84 ± 0.04	0.48 ± 0.11
$MAPbCl_3$	3.09 ± 0.10	2.97 ± 0.07	0.12 ± 0.12
$MAPbI_{2.1}Br_{0.9}$	1.96 ± 0.10	1.80 ± 0.02	0.16 ± 0.10
$MAPbI_{2.1}Cl_{0.9}$	2.64 ± 0.10	2.60 ± 0.05	0.04 ± 0.11
$MAPbBr_{1.5}Cl_{1.5}$	2.58 ± 0.10	2.44 ± 0.10	0.14 ± 0.14

Reports on both the materials $CH_3NH_3PbI_3$ and $CH_3NH_3PbBr_3$ clearly showed that the Br substitution instead of I yields the lower efficiency due to its wide bandgap. Even though they are wide bandgap materials, it can be employed in the tandem structure and light emission applications. Also it has good energy level matching with TiO_2, long charge carrier diffusion lengths, and low exciton binding energy.

While substituting Cl in this scenario leads to very wider bandgap value of 3.11 eV which restricts its use as the single light absorber [22]. The comparison of charge transport bandgap (E_g) with optical band gap (E_{opt}) with exciton binding energy. Table 2 shows the comparison of charge transport bandgap (Eg) with optical band gap (E_{opt}) with exciton binding energy. In that it can be clearly seen that only $MAPbI_3$ has the optimum bandgap closer to Shockley-Queisser limit.

1.4.2.2 Metal Substitution

In desire to construct the lead free perovskite solar cells, Sn a group 14 element with matching ionic radii was studied in place of Pb. In organic−inorganic layered Sn perovskites good electrical properties was studied, however optoelectronic was not explored. Interestingly in partial substitution of Pb which gives the stoichiometry of $CH_3NH_3Sn_xPb_{1-x}I_3$ in which high Sn

concentration reduced the bandgap. Also addition of Pb retarding the Sn^{2+} to Sn^{4+} oxidation state, which made the high efficiency while reduced carrier concentration. Also for using bismuth as the replacement for Pb, perovskite with the structure of $A_3B_2X_9$ should be introduced to suit its oxidation state. In comparison with Pb and Sn very less reports were made for Ge because of the highly oxidizing nature in moving up the periodic table. In the AMX_3 structure X-M-X plays the important role deciding the bandgap of the material. The measured bond angle for different metal cations are as follows 166.27(8)^o for Ge, 159.61(5)^o for Sn and 155.19(6)^o for Pb. Also decrease in the covalent character of M-I bond was found in going down the selection of metal cations. $AGeI_3 < ASnI_3 < APbI_3$ is the trend for increase in the bandgap for different metal cations. By combining Sn and Pb it is possible to fabricate NIR perovskite solar cells and still now IPCE curve of 1060 nm was reached [46].

Bismuth based perovskite, methylammonium iodobismuthate with molecular formula $(CH_3NH_3)_3Bi_2I_9$, (MBI) has been reported to be environment friendly and relatively more stable as compared to the lead halide perovskites. Apart from this, MBI possesses very good semiconducting, electronic, optical and ferroelectric properties along with the rich structural diversity. In MBI, the $6s^2$ lone pair from Bi^{3+} plays a crucial role in controlling all the physicochemical properties. However so far very negligible efficiency was obtained due to its wide bandgap.

1.4.2.3 Organic Cation Substitution

In ABX_3 perovskite structure monovalent cation is very crucial since it decides the structure, dimensionality, optoelectronic property and stability of the material. In 3D perovskite structure only small cations are permitted since it has the cuboctahedral cavity defined by four edge-sharing MX_6 octahedra. Goldschmidt tolerance factor (t) allows us to calculate the maximum ionic radii for the organic cation with stable structure. In cubic perovskite the tolerance factor ranges from 0.78 to 1.05 since it has a slight expansion due to its distorted structure, however the tolerance factor for exact cubic phase should be 1. Formamidinium is the only most studied organic cation in the place of methyl ammonium with tolerance factor of 0.99 which slightly higher than $CH_3NH_3PbI_3$ which is 0.91 [21].

In AMX_3 structure the cation A doesn't has any contribution in the band structure of the material it just act as charge compensation part in the crystal lattice. However, in MX_6 octahedron network it can affect the optical properties by variation of its size. Depending upon the size of the cation it could expand or contract the complete crystal lattice and cause the change in B–X bond length which has proved that highly important in deciding the bandgap of the material. The size of the cation A may not be larger than 2.6 Å since it should fit corner sharing metal octahedral crystal phase which may increase the tolerance factor in accordance with the size of the cation. Chances for the formation of lower dimensional or confined perovskite structure is possible if the cation size is too large.

So far three-dimensional (3D) perovskite structure with PbI_6 network can be formed with monovalent cations like K^+, Rb^+, Cs^+, methylammonium (MA^+), or formanidinium (FA^+). The ionic radius for Cs is minimum when compared to other organic cations and has the absorption at lower wavelength. From this phenomenon it can be clearly understood that cation A with larger size expected to expand the crystal lattice and reduce in the bandgap occurs [46].

1.5 Deposition techniques for lead based and lead free perovskites

1.5.1 Spin-coating technique (One step method)

In spin coating small amount of solution generally less than 1 ml was dropped on the desired substrate and then rotated in higher rpm for spreading the solution through the principle of centrifugal force. It is very simple and better method for solution crystal growth to form highly oriented layered perovskite structures by the evaporation of solvent. Spin coating also gives the flexibility to use different kinds of substrates like quartz, sapphire, silicon, plastic or glass. The parameters that controls the crystal growth mainly is the substrate temperature, type of solvent, and Rotation speed. For getting desired thickness in this one step methodology concentration of the precursor solution can be modified while keeping the rest all parameters fixed. Homogenous perovskite films even with less thickness of 10 to 100 nm can be can be easily achieved.

1.5.2 Two-step dip-coating

For two step methodology only metal halide films will be coated through spin coating or vacuum evaporation technique. After that by dipping in to the solution which contains organic cation the film will be converted to perovskite. Selecting the perfect solvent for making organic cation solution is very crucial since the organic cation should be soluble but final organic-inorganic perovskite should not soluble. Toluene/2-propanol are the solvents generally used for making perovskites in two step method. Depending on the system the dipping time varies from several seconds to few minutes.

1.5.3 Thermal evaporation technique

In 1997 M. Era et al used thermal evaporation at first for growing perovskites. Dual-source vapor deposition was performed by using lead iodide PbI_2 and organic ammonium iodide RNH_3I. On fused quartz substrates organic and inorganic source were co-evaporated and deposited. In the evaporation chamber pressure of 10^{-6} Torr was maintained. Vacuum deposited films were related to the spectra of single crystals while the spin coated films corresponds to the layered perovskites. The main advantage of this method is perovskites of smooth surface with controlled thickness can be precisely grown. It is often difficult to grow the perovskites with perfect stoichiometry. Due to the high possibility for each organic component may easily contaminate the system which limits the growth of different kinds of perovskites [20].

1.6 Problems in lead based perovskites and need of lead free light absorbers

1.6.1 Lead based perovskites

Structural diversity and tenability of optical band gap of perovskites have led to the attention of material scientists towards their huge application potentials [23]. Recent past had witnessed that lead based perovskites are very attractive in the field of photovoltaics [24] optoelectronics [25] and photolysis of water [26]. Application potential of perovskites in solar cell research geared huge attentions from year 2009 and within very short time frame it has attained the photo conversion efficiency up to 22.1% [27]. However, more attention is needed for realizing highly reproducible efficient perovskite solar cells. External power conversion efficiency of the such solar cells depends on optimization of various parameters like nature of perovskite materials [28], thickness of active layer [29], choice of hole transport materials [30] and so on. A highly

efficient perovskite solar cells basically requires controlled crystal growth with large crystal size with enhanced surface coverage. [31] Hysteresis in perovskite based solar cells is well known and utilization of bigger perovskite crystals had led to the achievement of minimum hysteresis index [32].

Optimized quantity and nature of chloride precursor for the attainment of large sized perovskite crystals with minimal disorder is still not clear. The impact of alkyl chain length of different alkyl ammonium chloride precursors on the crystal growth of $CH_3NH_3PbI_3$ is very crucial and also possibility to modify the surface smoothness with less defects makes this topic curious but there is no related studies in the literature.

1.6.2 Lead free perovskites

Recent past has witnessed the emergence of lead halide perovskites $MAPbX_3$ (MA = CH_3NH_3, X = I, Cl, Br) as potential candidate for the next generation solar cells opening the new possibility of low cost production while maintaining the high photo conversion (22.1%) [27]. This remarkable enhancement in the photo conversion efficiency could be credited to the fast pace development of efficient hole and electron transporting materials [33-34]. In spite of sky-rocketing success in the lead halide perovskites in such a short-time, currently Pb in this perovskite structure has become the matter of concern owing to its toxicity along with the high susceptibility to moisture. Therefore, it is indispensable to replace the Pb with other metal cations without altering the photovoltaic performance of the material. Owing to diminished toxicity of Sn and Bi along with the matching ionic radius to form perovskite structure they are strong contender to replace the Pb. Recent investigations in this regards towards the replacement of Pb by Sn have raised the serious issue on the environmental stability [35] and reduced photovoltaic performance [36]. These issues have led to the search for other alternate materials and Bi metal has gained a good deal of attention from the material science community.

Park et al. [37] have reported Bi based organic-inorganic hybrid perovskites having chemical structure $A_3Bi_2I_9$ (A= CH_3NH_3 or Cs) by replacing Pb with Bi and used as active component for the perovskite solar cells. Unfortunately, large number of defect states and large optical bandgap (about 2.1~2.4 eV) of this material resulted in to very poor photo conversion efficiency. Lyu et al.[47] have also investigated MBI based solar cells and its fundamental

properties, but due to background carrier concentration, low carrier mobility and wide bandgap resulted in to very poor efficiency (0.2 %). Oz et al. [38] have also employed zero-dimensional MBI for photovoltaic application but ended up with negligible efficiency of 0.1 % due to the wide bandgap (2.9 eV). A perusal of these reports clearly corroborates that bandgap tuning of MBI is mandatory in order to realize the improved photovoltaic performance. Therefore, development of Bi based perovskite by replacing Pb with Bi without disturbing the basic properties of lead halide perovskites is highly desired.

1.7 Challenges and ideas to overcome

Even though addition of chloride has the huge impact on the crystal growth and surface morphology in lead halide perovskites. Addition of chloride from different precursors like $PbCl_2$ [39], and Methyl ammonium chloride [40] has the variation in impact on the lead halide perovskites. Different kind of chloride precursors resulted in different morphology and device performances from the literature. So, our plan to overcome this challenge is to use different chloride precursors to optimize the suitable precursor and also to compare the effect alkyl chain length over this process. After optimizing the suitable chloride precursor in one step method implying them in two step method may give more controlled crystal growth with smooth surface.

In the case of lead free (bismuth based perovskites) for reducing the optical bandgap many efforts have been made like organic cation $CH_3NH_3^+$ was replaced by NH_4^+, however the measured bandgap was 2.04 eV [41]. Double perovskite structure $Cs_2AgBiBr_6$ was studied by slavney et al [42] but still the measured bandgap was 1.95 eV. A perovskite with structure $MABiSI_2$ [43] using split anion approach was theoretically studied but practically not yet proved. So, in this case our plan is to exploit the voids in between metal halide $(Bi_2I_9)^{3-}$ octahedra layers as the interstitial sites for the doping agent. We chose sulfur as the doping agent with ionic radii of 0.37 Å which is almost six times lesser than the ionic radii of iodine is 2.2 Å because in this scenario sulfur cannot replace iodine however it has the possibility to accommodate itself in the interstitial sites.

1.8 References

1) Energy, Renewable. "Types of Renewable energy." Retrieved on November 5 (2011): 2011.

2) http://www.ucsusa.org/clean_energy/our-energy-choices/renewable-energy/how-biomass-energy-works.html#.WAOpivl970M

3) Gipe, Paul. Wind energy basics. Chelsea Green Pub. Co., 2009.

4) http://energy.gov/eere/energybasics/articles/hydrogen-fuel-basics

5) http://www.renewableenergyworld.com/ocean-energy/tech.html

6) EREC. European Renewable Energy Council: Renewable energy target for Europe – 20% by 2020. (Brief Paper, Brussel); 2005 (https://ec.europa.eu/energy/en/topics/renewable-energy).

7) ESTIF. European Solar Thermal Industry Federation (ESTIF). Solar thermal markets in Europe, Brussel. 2006.

8) Othman AK, Jakhrani AQ, Abidin WAWZ, Zen H, Baharun A. Malaysian Government Policy. In: Renewable Energy: Solar PV System, in World Engineering Congress 2010, 2nd–5th August 2010, C.o.N.R.a.G. Technology, Editor. 2010, The Federation of Engineering Institutions of Islamic Countries: Kuching, Sarawak, Malaysia; 2010.

9) Solangi, K. H., et al. "A review on global solar energy policy." Renewable and sustainable energy reviews 15.4 (2011): 2149-2163.

10) Miles, R. W., K. M. Hynes, and I. Forbes. "Photovoltaic solar cells: An overview of state-of-the-art cell development and environmental issues."Progress in Crystal Growth and Characterization of Materials 51.1 (2005): 1-42.

11) Ghosh, M., et al., In Proceedings of the 19th European Photovoltaic Solar Energy Conference, Paris, France, (2004), 560.

12) C.R. Wronski, D.E. Carlson Amorphous Si Solar Cells M.D. Archer, R. Hill (Eds.), Clean Electricity from Photovoltaics, Imperial College Press, London, UK (2001), p. 199.

13) R.H. Bube Photovoltaic Materials, Imperial College Press, London, U.K. (1998).

14) Miles, Robert W., Guillaume Zoppi, and Ian Forbes. "Inorganic photovoltaic cells." Materials today 10.11 (2007): 20-27.

15) Green, Martin A., et al. "Solar cell efficiency tables (Version 45)." Progress in photovoltaics: research and applications 23.1 (2015): 1-9.
16) Abdulrazzaq, Omar A., et al. "Organic solar cells: a review of materials, limitations, and possibilities for improvement." Particulate science and technology 31.5 (2013): 427-442.
17) Zhang, Shufang, et al. "Highly efficient dye-sensitized solar cells: progress and future challenges." Energy & Environmental Science 6.5 (2013): 1443-1464.
18) Grätzel, Michael. "Dye-sensitized solar cells." Journal of Photochemistry and Photobiology C: Photochemistry Reviews 4.2 (2003): 145-153.
19) Jung, Hyun Suk, and Nam-Gyu Park. "Perovskite solar cells: from materials to devices." Small 11.1 (2015): 10-25.
20) Kandjani, Sohrab Ahmadi, Soghra Mirershadi, and Arash Nikniaz. "Inorganic–Organic Perovskite Solar Cells." (2015).
21) Boix, Pablo P., et al. "Perovskite solar cells: Beyond methylammonium lead iodide." The journal of physical chemistry letters 6.5 (2015): 898-907.
22) Kazim, Samrana, et al. "Perovskite as light harvester: a game changer in photovoltaics." Angewandte Chemie International Edition 53.11 (2014): 2812-2824.
23) Eperon, Giles E. "Formamidinium lead trihalide: a broadly tunable perovskite for efficient planar heterojunction solar cells." Energy & Environmental Science 7.3 (2014): 982-988.
24) Kojima, Akihiro, "Organometal halide perovskites as visible-light sensitizers for photovoltaic cells." Journal of the American Chemical Society131.17 (2009): 6050-6051.
25) Pedesseau, Laurent, "Electronic properties of 2D and 3D hybrid organic/inorganic perovskites for optoelectronic and photovoltaic applications."Optical and Quantum Electronics 46.10 (2014): 1225-1232.
26) Luo, Jingshan, "Water photolysis at 12.3% efficiency via perovskite photovoltaics and Earth-abundant catalysts." Science 345.6204 (2014): 1593-1596.
27) http://www.nrel.gov/ncpv/.
28) Koh, Teck Ming, "Formamidinium-containing metal-halide: an alternative material for near-IR absorption perovskite solar cells." The Journal of Physical Chemistry C 118.30 (2013): 16458-16462.

29) Xiao, Zhengguo, "Efficient, high yield perovskite photovoltaic devices grown by interdiffusion of solution-processed precursor stacking layers."Energy & Environmental Science 7.8 (2014): 2619-2623.

30) Jeon, Nam Joong, "o-Methoxy substituents in Spiro-OMeTAD for efficient inorganic–organic hybrid perovskite solar cells." Journal of the American Chemical Society 136.22 (2014): 7837-7840.

31) Im, Jeong-Hyeok, "Growth of $CH_3NH_3PbI_3$ cuboids with controlled size for high-efficiency perovskite solar cells." Nature nanotechnology 9.11 (2014): 927-932.

32) Kim, Hui-Seon, and Nam-Gyu Park. "Parameters affecting I–V hysteresis of $CH_3NH_3PbI_3$ perovskite solar cells: effects of perovskite crystal size and mesoporous TiO2 layer." The Journal of Physical Chemistry Letters 5.17 (2014): 2927-2934.

33) Yu, Z.; Sun, L. Recent Progress on Hole-Transporting Materials for Emerging Organometal Halide Perovskite Solar Cells. Adv. Energy Mater. 2015, 5, 1500213.

34) Völker, S. F.; Collavini, S.; Delgado, J. L. Organic Charge Carriers for Perovskite Solar Cells. ChemSusChem. 2015, 8, 3012–3028.

35) Hao, F.; Stoumpos, C. C.; Cao, D. H.; Chang, R. P. H.; Kanatzidis, M. G. Lead-Free Solid-State Organic–inorganicHalide Perovskite Solar Cells. Nat. Photonics 2014, 8, 489–494.

36) Noel, N. K.; Stranks, S. D.; Abate, A.; Wehrenfennig, C.; Guarnera, S.; Haghighirad, A.-A.; Sadhanala, A.; Eperon, G. E.; Pathak, S. K.; Johnston, M. B.; Petrozza, A.; Herz, L. M.; Snaith, H. J. Lead-Free Organic-Inorganic Tin Halide Perovskites for Photovoltaic Applications. Energy Environ. Sci. 2014, 7, 3061–3068.

37) Park, B.-W.; Philippe, B.; Zhang, X.; Rensmo, H.; Boschloo, G.; Johansson, E. M. J. Bismuth Based Hybrid Perovskites $A_3Bi_2I_9$ (A: Methylammonium or Cesium) for Solar Cell Application. Adv. Mater. 2015, 27, 6806–6813.

38) Oz, S.; Hebig, J. C.; Jung, E.; Singh, T.; Lepcha, A.; Olthof, S.; Jan, F.; Gao, Y.; German, R.; van Loosdrecht, P. H. M.; Meerholz, K.; Kirchartz, T.; Mathur, S. Zero-Dimensional $(CH_3NH_3)_3Bi_2I_9$ Perovskite for Optoelectronic Applications. Sol. Energy Mater. Sol. Cells. doi: 10.1016/j.solmat.2016.01.035.

39) Pool, Vanessa L., et al. "Chlorine in $PbCl_2$ derived hybrid-perovskite solar absorbers." Chemistry of Materials 27.21 (2015): 7240-7243.

40) Dar, M. Ibrahim, et al. "Investigation regarding the role of chloride in organic–inorganic halide perovskites obtained from chloride containing precursors."Nano letters 14.12 (2014): 6991-6996.

41) Sun, S.; Tominaka, S.; Lee, J.-H.; Xie, F.; Bristowe, P. D.; Cheetham, A. K. Synthesis, Crystal Structure, and Properties of a Perovskite-Related Bismuth Phase, $(NH_4)_3Bi_2I_9$. APL Mater. 2016, 4, 031101.

42) Slavney, A. H.; Hu, T.; Lindenberg, A. M.; Karunadasa, H. I. A Bismuth-Halide Double Perovskite with Long Carrier Recombination Lifetime for Photovoltaic Applications. J. Am. Chem. Soc. 2016, 138, 2138–2141.

43) Sun, Y.; Shi, J.; Lian, J.; Gao, W.; Agiorgousis, M. L.; Zhang, P.; Zhang, S. Discovering Lead-Free Perovskite Solar Materials with Split-Anion Approach. Nanoscale 2016, 8, 6284-6289.

44) Li, Chi, et al. "Halide-substituted electronic properties of organometal halide perovskite films: direct and inverse photoemission studies." ACS applied materials & interfaces 8.18 (2016): 11526-11531.

46) Yusoff, Abd Rashid bin Mohd, and Mohammad Khaja Nazeeruddin. "Organohalide Lead Perovskites for Photovoltaic Applications." The journal of physical chemistry letters 7.5 (2016): 851-866.

46) Gao, Peng, Michael Grätzel, and Mohammad K. Nazeeruddin. "Organohalide lead perovskites for photovoltaic applications." Energy & Environmental Science 7.8 (2014): 2448-2463.

47) Lyu, Miaoqiang, et al. "Organic–inorganic bismuth (III)-based material: A lead-free, air-stable and solution-processable light-absorber beyond organolead perovskites." Nano Research 9.3 (2016): 692-702.

Chapter 2. INSTRUMENTATION & CHARACTERIZATION

2.1 X-ray diffraction (XRD) analysis

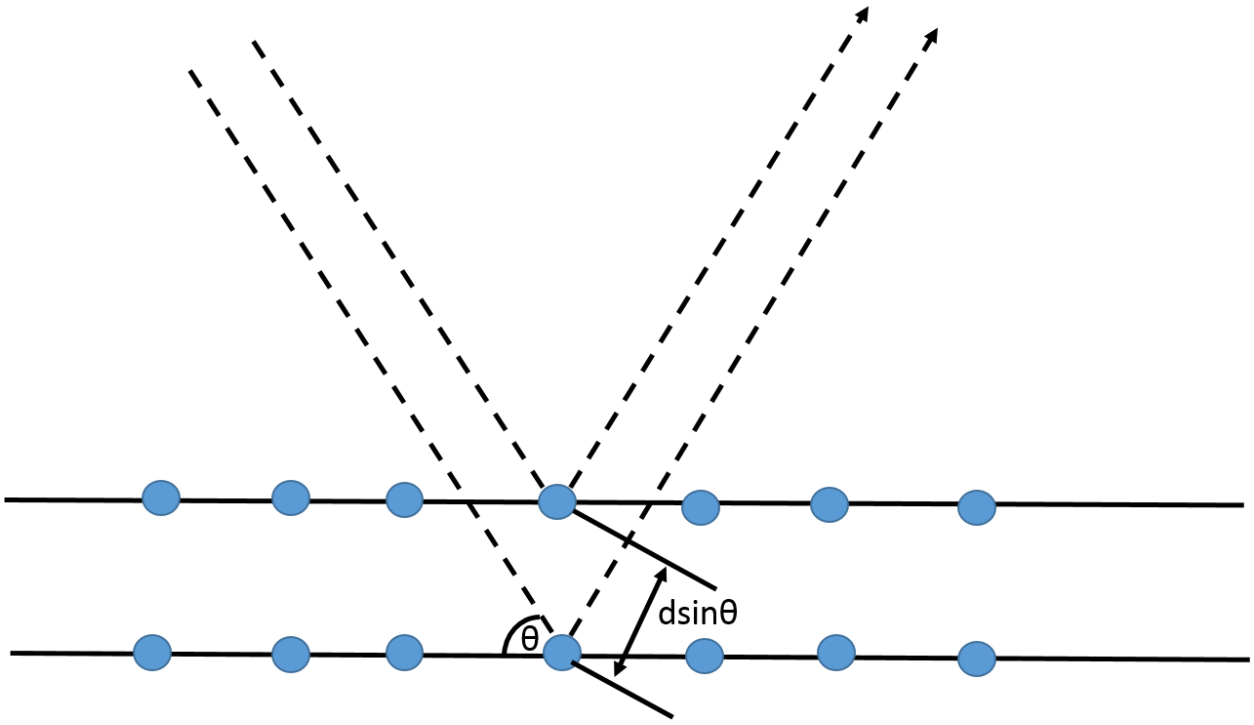

Figure 1. Bragg diffraction

X-ray powder diffraction (XRD) is the best analytical technique used widely for the structural characterization and can provide information on the dimensions of unit cell of the materials. In identifying the structure or phase of the material peaks position and intensity plays the crucial role. For example in the case of graphite XRD pattern will be different when compared to that of diamond even though they made up of carbon atoms. So, in terms of physicochemical properties of the materials this phase variation plays the vital role. In the crystalline materials like minerals, regular and repeating planes of atoms forms the three dimensional crystal lattice. So, when X-rays that are generated by the X-ray tube focused on these crystalline materials (planes of

atoms) some part of the beam is transmitted, some part is absorbed by the material, few parts refracted while some parts will be diffracted.

Figure 1 shows the Bragg diffraction occur when two identical wavelength and phase approach the crystalline materials that is scattered by two different atoms. X-ray diffraction pattern strongly depends on the types of atoms that makes the crystal lattice and on the arrangement of this atoms. From the diffracted X-ray beam inter planar distance between the atoms can be calculated using the Bragg's Law which is given in equation 1.

$$n\lambda = 2d \sin\theta \qquad \rightarrow (1)$$

Where n is the order of the diffracted beam, λ is the wavelength of the X-ray, d is the distance between the planes generally called d-spacings. These d-spacings are like fingerprints of the materials, it's unique and different for every materials. When the obtained d-spacing values are compared with standard data as reference like International Centre for diffraction data (ICDD) or JCPDS the fingerprint allows us to identify the particular material [1].

In XRD the X-rays are produced within a sealed tube which is under vacuum. Total number of electrons that are generated from the tube depend on the total current supplied to the filament with the voltage of 15-60 KV. This high voltage accelerates the electrons which hits the target generally copper. When the electron travels in high velocity hits the target and X-rays are produced. So, wavelength of the X-rays are depend on the type of target material we use that will be guided to hit the samples. The diffracted X-ray signal is collected through the detector which will be converted to a count rate electronically. X-ray scan generally represents the change in angle maintained between the X-ray source, the sample, and the detector at a controlled rate. Amorphous materials also can be easily recognized by the absence of peaks. Similarly for studying the bulk materials and thin films too. XRD has the wide application in diverse fields like material science, chemistry, environmental science, geology, forensic science, and the pharmaceutical industry. Various parameters like crystallite size, lattice parameters, lattice stress and strain, and phase transition can be studied through XRD [2].

2.2 X-ray photoelectron spectroscopy (XPS)

X-ray photoelectron spectroscopy (XPS) is a technique used to analyze a sample to the depth of 2 to 5 nm which comes under the tools for surface characterization. XPS was developed by Kai Siegbahn in 1960s. XPS technique is used to identify the elements present in the surface and also to find the nature of bonding between the existing elements. The drawback of XPS is it cannot detect hydrogen and helium but except these it can detect all other elements.

Ultrahigh vacuum (UHV) around 10^{-9} millibar is required for the operation of XPS. In a UHV chamber one-trillionth that of air per unit of volume exist when the atmospheric pressure is

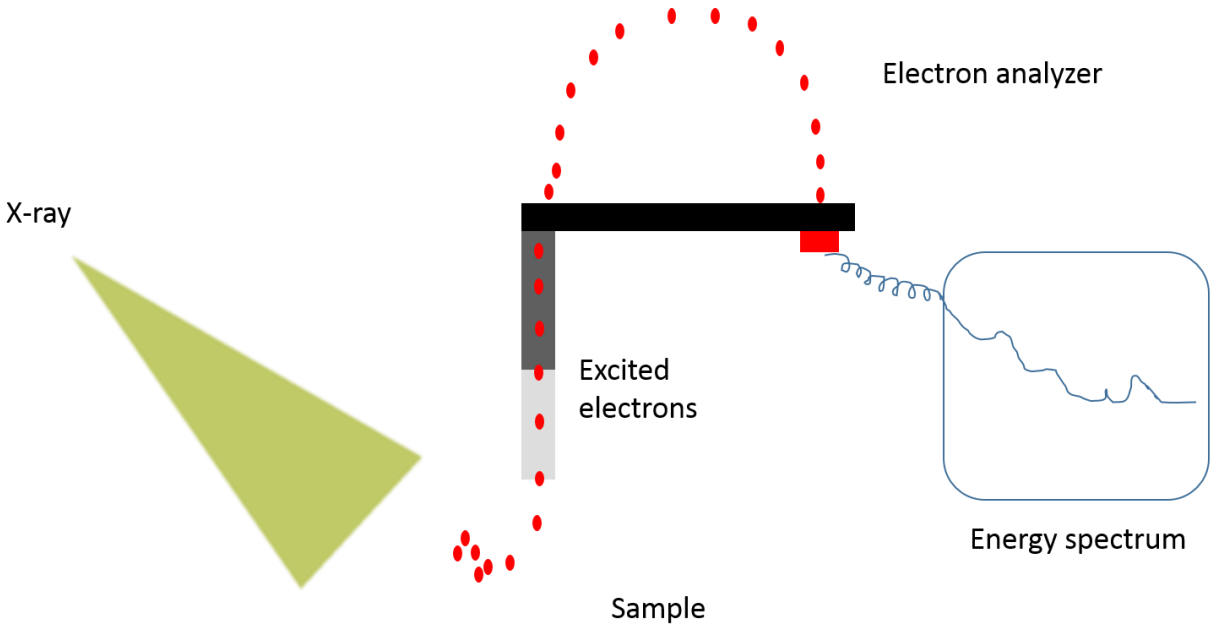

Figure 2. Working principle of XPS

around 1 bar, such a high vacuum is required because any impurities like O_2 or H_2O present can make error in the measurement. This UHV in the chamber protects the sample from degradation and give the precise surface investigation using XPS. When the sample is irradiated with the X-ray with sufficient energy specific electron in the bound states is excited. Enough energy is provided by the X-rays to exit the photoelectrons which attracted by the nuclear force of an element. The key features of XPS is even the electrons ejected from specific core levels have the little shift based on the valence configuration of the material. Another key feature is the transition of electrons at core level occurs at specific energy which is the particular binding energy. From this the particular element can be easily identified [3].

Figure 2 shows the typical construction and working principle of the XPS instrument. In XPS the few photo ejected electrons randomly scatters from the sample surface, while other electrons without any energy loss escapes from the surface of the sample to vacuum. Once it reached the vacuum the electron will be collected and the corresponding kinetic energy is measured by electron analyzer. An electron analyzer then plots the relative energy spectrum (total amount of electrons versus time) versus the binding energy (energy of the electrons in the atom). In addition to identifying the elements, intensity of the peaks can say the total amount of the particular element present in the sample. Also by measuring the total area of the particular peak (contribution of each peak area) can give the total number of atoms present in the measured sample [4].

2.3 Ultraviolet-visible (UV-vis) spectroscopy

Generally spectrophotometry is used to determine the concentration of the sample by observing the absorbance of light by the sample. So, ultraviolet-visible (UV-vis) spectroscopy is the technique which uses the light in ultraviolet and visible region to analyze the samples. The energy of the light given in this region cause the electrons in lower energy level to excite to higher energy state at specific wavelength for particular molecule. When the beam of light is irradiated to the analyte some part of the photons may be absorbed while remaining can be transmitted through the sample. The ratio of the light intensity (Io) which is entering the sample to that of light makes the sample excited (I) at specific wavelength is called transmittance(T). The negative logarithm of the transmittance is called absorbance (A) of the sample [5].

$$A = - \log (T) \qquad \rightarrow (2)$$

The amount of light absorbed by the sample depends on the material absorptivity (ε), the path length (b), and the concentration of the sample (c). From this in terms of concentration units of molarity, Beer-Lambert law can be explained as

$$A = \varepsilon * b * c \qquad \rightarrow (3)$$

Where ε is the wavelength-dependent molar absorptivity coefficient with units of M^{-1} cm^{-1}. As we ε and b are constant, which clearly states that absorption of light is directly proportional to the

concentration of the analyte. The main prerequisite for Beer Lambert law are i) Homogenous absorbing medium in the interaction volume. ii) No scattering in the radiation should be there in the absorbing medium iii) Monochromatic light must be the incident radiation on the sample [6].

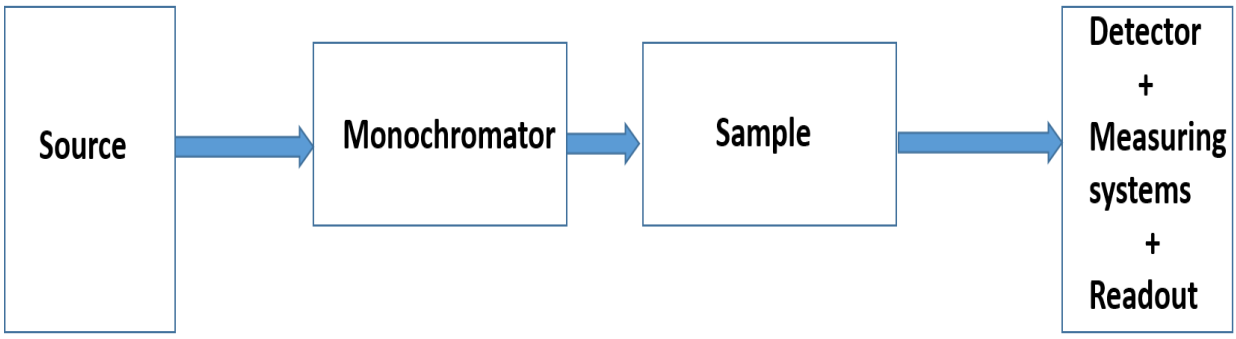

Figure 3. Construction of Ultraviolet-visible (UV-vis) spectroscopy

Figure 3 show the basic construction of Ultraviolet-visible (UV-vis) spectroscopy. First block is the light source section, here usually for the visible region tungsten lamp and deuterium or hydrogen lamp for ultraviolet wavelengths is used. For producing the beam of monochromatic light which can be selected from wide wavelength monochromator is used. In sample section cuvettes are used to carry the analyte that are placed in the light path. Glass and plastics has the strong absorption below 310 nm so it cannot be used for materials has the absorption at that region. Similarly silicon can be used for the materials has its absorption in ultraviolet region since they transparent for the wavelength above 180 nm. As the detector silicon diode, photomultiplier, or the diode array are generally used [7].

2.4 Photoacoustic spectroscopy (PAS)

Alexander Graham Bell discovered the photoacoustic effect and based on this effect photoacoustic spectroscopy measurement was introduced. In photoacoustic spectroscopy when light is irradiated on the sample it emits acoustic waves which is similar to the light pulse frequency. Highly-sensitive microphones and other advances in electronics made possible to design this

instrument for characterization especially gas samples. By the improvement in FTIR instruments recently it is possible to even in the IR region using the photoacoustic spectroscopy for solid samples.

In a sealed vessel solid sample is placed to which microphone is attached. Heat is generated on the sample due to the absorption modulated IR light that is irradiated. High sensitivity microphone which is place near the sample detects the change in pressure of surrounding gaseous layer caused by the heat produced on the sample. Acoustic interference waves from the microphone are converted signal similar to the absorption spectrum using Fourier transformation. The theoretical explanation for photoacoustic spectroscopy has variation depends on the state of the sample and instrument construction. However, RG theory which is based on thermal diffusion can explain the theory for solid samples [8].

RG theory was developed based on the photoacoustic signal, sample thickness l, light absorption length 1/ß where ß is the absorbance coefficient, and thermal diffusion length $1/a_s$ where a_s is the thermal diffusion coefficient. When the sample is optically opaque and thermally thick photoacoustic signal highly depends on the thermal diffusion length and sample absorption. The major advantages of photoacoustic spectroscopy when compared to other absorption spectroscopy are i) With short path length highly sensitive in gas analysis ii) High absorption coefficients can be measured even for opaque samples with high concentration iii) Solid samples like powder, thin films, and bulk solids can be measured. iv) Light scattering in photoacoustic spectroscopy cause less effect over the other absorption measurement [9].

2.5 Fourier transform IR spectroscopy (FTIR)

In IR spectroscopy low concentration measurements in ambient atmosphere has several limitations like presence of humidity, carbon dioxide and methane cause the error in the measurements. Also sensitivity is very low in small concentrations below ppm level. Also subtracting background noise is very difficult in IR spectroscopy. So, FTIR (Fourier transform IR spectroscopy) was developed with high analytical capabilities to trace the impurities in ambient atmosphere. It have several merits over IR spectroscopy like high sensitivity in less amount of analyte with speed and improved data processing.

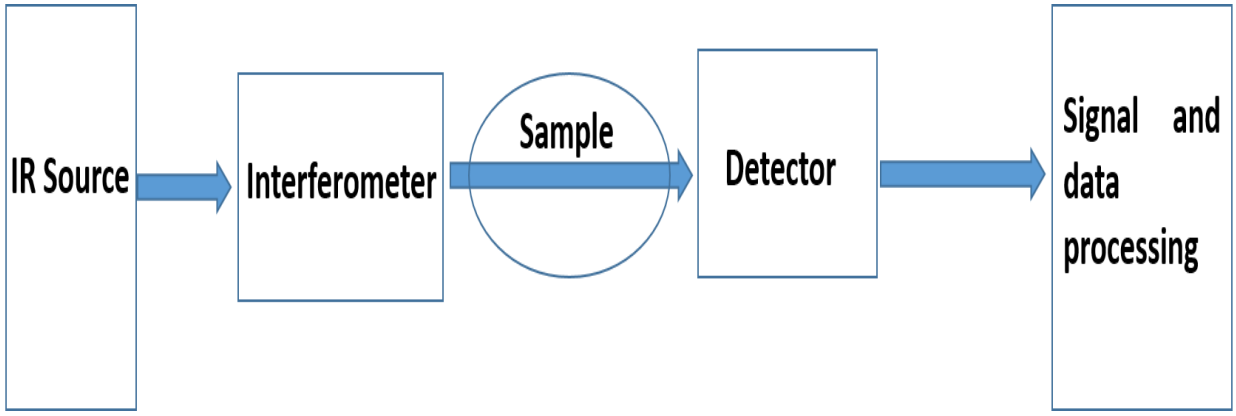

Figure 4. Basic components of FTIR

The basic components of FTIR is shown in the figure 4. Broad band of different wavelength in IR region is emitted by the IR source. Temet GASMET FTIR CR-series is a SiC ceramic at a temperature of 1550 K is used as the IR source. The IR radiation is modulated by the interferometer

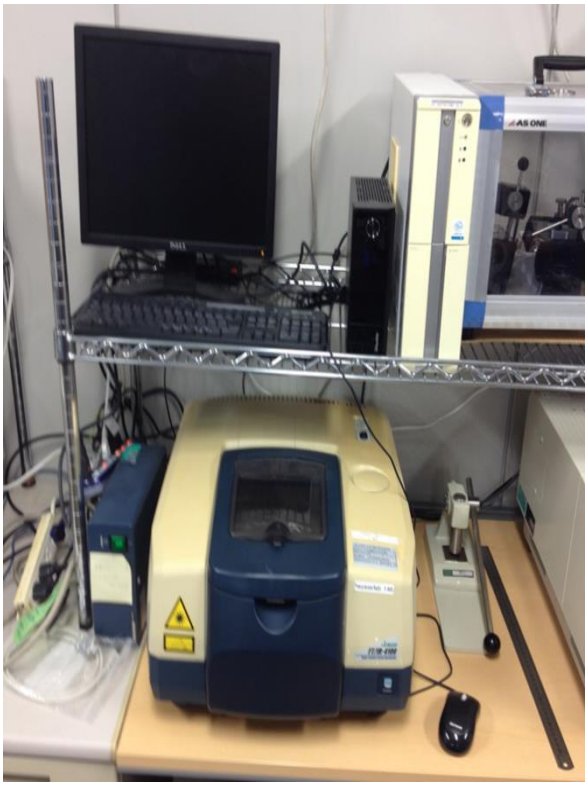

Figure 5. Fourier transform Infrared spectrometer used in this present work.

and it also performs the Fourier transform on the entering IR radiation. When those modulated IR beam enters the sample it is absorbed at various wavelengths by the corresponding molecule present in the sample. Liquid-nitrogen cooled MCT (Mercury-Cadmium-Telluride) is used as the detector to measure the intensity of the incoming IR beam. The electronic setup is used to convert the detected signal numerically for the given sample. Interferometer is very crucial part in FTIR spectrometer. Before entering the beam splitter the IR radiation is collected and collimated [10]. Figure 5 shows the Fourier transform Infrared (FTIR) spectrometer used in this present work.

Depending on the characteristic bonds present in the sample specific frequency is absorbed. After the incidence of IR light the molecule starts to vibrate and resonance based on the bonds or functional groups present in the sample due to the absorption of specific frequency of light. Thus the characteristic of the particular function group and nature of the bonds can be easily studied through specific absorbed vibration frequency [11]. FTIR was used in the present study to find the organic impurities in the sample related to xanthate groups since we used metal xanthate as one of the precursor.

2.6 Thermogravimetric analysis (TGA)

In a controlled atmosphere with controlled temperature program the mass of a substance is monitored as a function of temperature or time is known as thermogravimetric analysis (TGA). While heating the sample weight of the corresponding material either increases or decreases [12]. Sample pan is placed over the precision balance in TGA setup. After that sample inside the furnace is allowed to heat or cool during the experiment. Inert or a reactive gas is purged inside the chamber for controlling sample environment. TGA graph is plotted between the percentage of weight loss with respect to temperature or time. Final product after decomposition is known from the total weight loss percentage. The decomposition temperature is determined from the temperature at which decrease in percentage mass curve is observed. For metal xanthates corresponding decomposition temperature was studied through TGA in present work and also the decomposition temperature was verified by other techniques too. Mainly we used this technique for finding the post annealing temperature for our samples with metal xanthates [13]. Figure 6 shows the thermogravimetric analysis apparatus used in the present thesis.

Figure 6. Thermogravimetric analysis apparatus used in this present thesis.

2.7 Field Emission Scanning Electron Microscopy (FESEM)

The field emission scanning electron microscope (FE-SEM) uses the high-energy beam electrons to image the sample surface by raster scanning. The atoms in the sample interacts with the electron beam which produces the signal that contains the information about the topography, composition, and other properties. Thermionic emitter and field emitter are the two types of emission source used. Usage of this specific emitter makes the difference between Scanning Electron Microscope (SEM) and the Field Emission Scanning Electron Microscope (FE-SEM) [14]. Lanthanum hexaboride and tungsten are the materials used make the filament which is heated by the thermionic emitters. Thermal drift during operation, evaporation of cathode material, and low brightness are the drawbacks in thermionic sources which can be overcome by the field emission type. In field emission instead of heating the filament high electrical potential gradient is produced. Secondary electron detection is also possible due to the development of field emission

source. The apparatus functions at high vacuum around 10^{-6} Pa and the voltage range between the cathode and anode is in the order of 0.5 to 30 kV [15].

Figure 7. FE-SEM used in the present work

FE-SEM has various applications like i) In thin films thickness measurements ii) Cross section view to find the thickness of different interface (In the case of more than one layer) iii) To determine surface morphology and iv) To study grain and grain boundary. In our case FE-SEM was employed to study the surface morphology of lead based and lead free perovskites especially to check the surface coverage over the mesoporous TiO_2. Presence of pin holes and homogenous surface of the samples also studied for the perovskites. Figure 7 shows the FE-SEM used in the present work.

2.8 scanning probe microscopy (SPM)

The main advantage of SPM over FE-SEM and TEM is the sample will not be damaged due to slicing or thin cutting. Another advantage is three dimensional image can be obtained from the SPM also no vacuum is required. Scanning Tunneling Microscopes (STMs) and Atomic Force Microscopes (AFMs) are the two main types of SPM. In the case of STM fine metal tip around 1-10 nm is made to scan the surface. Only conducting samples can be measured using STM. Because

the metal tip is connected to voltage supply and when it is brought near to the sample current flows which is called as tunnel current. So, nonconducting samples cannot be measured using this samples [16].

In the case of AFM thin beam of laser beam is used as the sensor at the fine tip and so called cantilever. The beam of laser is focused on to the upper part of the cantilever while the reflected beam is collected by the detector. By the bending of cantilever over the surface gives the information regarding the surface roughness, and morphology. But the cantilever is few microns length and very less in thickness than length. So, force on the cantilever should be handled with huge care. Unlike STM, AFM can also be used on characterizing insulating material. Two kinds of mode is present in the AFM i) Contact mode or DC mode and ii) Tapping mode or AC mode. In contact mode the cantilever is made to move up and down on the surface of the sample and mechanical movement was the detected using the detector. In the present work AFM was used in the contact mode to study the roughness and homogeneity of the perovskite film. Rough surface is not good for the solar cell fabrication since it results in non-uniform interfaces with hole transporting material [16] [17]. Figure 8 shows the SPM used in the present work.

Figure 8. SPM used in the present work

2.9 References

1. Stanjek, H., and W. Häusler. "Basics of X-ray Diffraction." *Hyperfine Interactions* 154.1-4 (2004): 107-119.
2. Borisenko, Victor. *Semiconducting Silicides: Basics, Formation, Properties*. Vol. 39. Springer Science & Business Media, 2013.
3. Andrade, Joseph D. "X-ray photoelectron spectroscopy (XPS)." *Surface and interfacial aspects of biomedical polymers*. Springer US, 1985. 105-195.
4. Turner, Noel H., Brett I. Dunlap, and Richard J. Colton. "Surface analysis: x-ray photoelectron spectroscopy, Auger electron spectroscopy and secondary ion mass spectrometry." *Analytical Chemistry* 56.5 (1984): 373R-416R.
5. Fuwa, Keiichiro, and B. L. Valle. "The Physical Basis of Analytical Atomic Absorption Spectrometry. The Pertinence of the Beer-Lambert Law." *Analytical Chemistry* 35.8 (1963): 942-946.
6. Swinehart, D. F. "The beer-lambert law." *J. Chem. Educ* 39.7 (1962): 333.
7. Zhang, Jin Z. *Optical properties and spectroscopy of nanomaterials*. Singapore: World Scientific, 2009.
8. Sawada, T., S. Oda, and K. Washio. "Hikari Onkyou Bunkouhou To Sono Ouyou—PAS—." *Japan Scientific Societies Press, Tokyo* (1982).
9. Bageshwar, Deepak V., et al. "Photoacoustic Spectroscopy and Its Applications–A Tutorial Review." *Eurasian Journal of Analytical Chemistry*5.2 (2010): 187-203.
10. Siesler, Heinz W., et al., eds. *Near-infrared spectroscopy: principles, instruments, applications*. John Wiley & Sons, 2008.
11. Ferrari, Marco, Leonardo Mottola, and Valentina Quaresima. "Principles, techniques, and limitations of near infrared spectroscopy." *Canadian journal of applied physiology* 29.4 (2004): 463-487.
12. Gabbott, Paul, ed. *Principles and applications of thermal analysis*. John Wiley & Sons, 2008.
13. Haines, Peter J. *Principles of thermal analysis and calorimetry*. Royal society of chemistry, 2002.

14. Goldstein, Joseph, et al. *Scanning electron microscopy and X-ray microanalysis: a text for biologists, materials scientists, and geologists*. Springer Science & Business Media, 2012.
15. Bonard, Jean-Marc, et al. "Field emission of individual carbon nanotubes in the scanning electron microscope." *Physical review letters* 89.19 (2002): 197602.
16. Wiesendanger, Roland. *Scanning probe microscopy and spectroscopy: methods and applications*. Cambridge University Press, 1994.
17. Loos, Joachim. "The art of SPM: Scanning probe microscopy in materials science." *Advanced Materials* 17.15 (2005): 1821-1833.

Chapter 3. Effects of different chloride precursors on crystal growth of lead halide perovskites

3.1 Introduction

Perovskite materials have the huge application in various fields since their structure is more comfortable to tune its optical band gap. [1] Especially lead based perovskites attracted the researchers in the field of photovoltaics, [2] optoelectronics, [3] and also recently in water photolysis.[4] After the hard research perovskite solar cells have attained the maximum efficiency up to 22.1%. [5, 6] However, more attention is needed for realizing the highly reproducible efficient perovskite solar cell. Although the efficiency of the solar cells depends on the various parameters like perovskite materials, [7] thickness, [8] HTL materials [9-11] and so on, highly efficient perovskite solar cells basically requires controlled crystal growth and more surface area coverage. [12] Efforts have been made to enhance and control the crystallization of perovskite by different ways such as changing the solution composition, [13, 14] by adding additives, [15] solvent engineering [16] etc. In addition to that incorporation of chloride ions in $MAPbI_3$ also plays the vital role in the crystallization process. [17, 18] Hysteresis in perovskite based solar cells is well known and utilization of bigger perovskite crystals had led to the achievement of minimum hysteresis index [19].

$MAPbI_{3-x}Cl_x$ is the important candidate suitable for planar architecture in solar cells [20] and also have very good photoluminescence property [21]. Addition of chloride ions highly enhances the carrier life time [22], diffusion length [20], crystal formation [23] and film morphology [24] in $MAPbI_3$. Incorporation of chloride ions in $MAPbI_3$ is the very critical issue even though it doesn't affect the optical band gap and crystal structure of the perovskite material. Mixed halide perovskite ($MAPbI_{3-x}Cl_x$) has been prepared by incorporating $PbCl_2$ and has been used in the field of photovoltaics [25] and to elucidate the role of chloride ions [23]. Zhao et al. [26] concluded that crystallization of the perovskite crystal improves by the addition of MACl due to the formation of intermediate structure ($MAPbCl_3$) which disappears after annealing. Williams et al. [24] emphasized that topo tactic self-assembly driven phase transformation induced by the presence of chloride ion has the huge impact on the crystallization behavior of the perovskite

crystals. Unfortunately, in this work morphology and film coverage was different for $PbCl_2$ and MACl additives due to the differences in solution based aggregation which poses the obvious questions about the choice of the optimum chloride precursor. Zuo et al. [27] achieved fill factor (FF) of 80.11% using NH_4Cl as the precursor for chloride ion. Although the actual role of chloride ions in controlling the crystal growth of $MAPbI_3$ is still not completely clear but it is believed that chloride ions enhances the crystal growth of $MAPbI_3$ without entering in to the crystal lattice[23]. Thus it is important to find out the optimum precursor of chloride ions in order to achieve larger perovskite crystals with minimum disorder. In the present work, it has been found that crystallization behavior of the perovskites formed varied with different chloride precursors and ethyl ammonium chloride (EACl) was one of best choice to give perovskite grains with large size and minimum crystal disorder. To the best of our knowledge there are no reports about the comparative study of different chloride precursors in controlling the growth of the $MAPbI_3$ perovskite crystals. One step method to prepare perovskite crystals which is relatively simpler with controlled crystal growth is highly demanded.

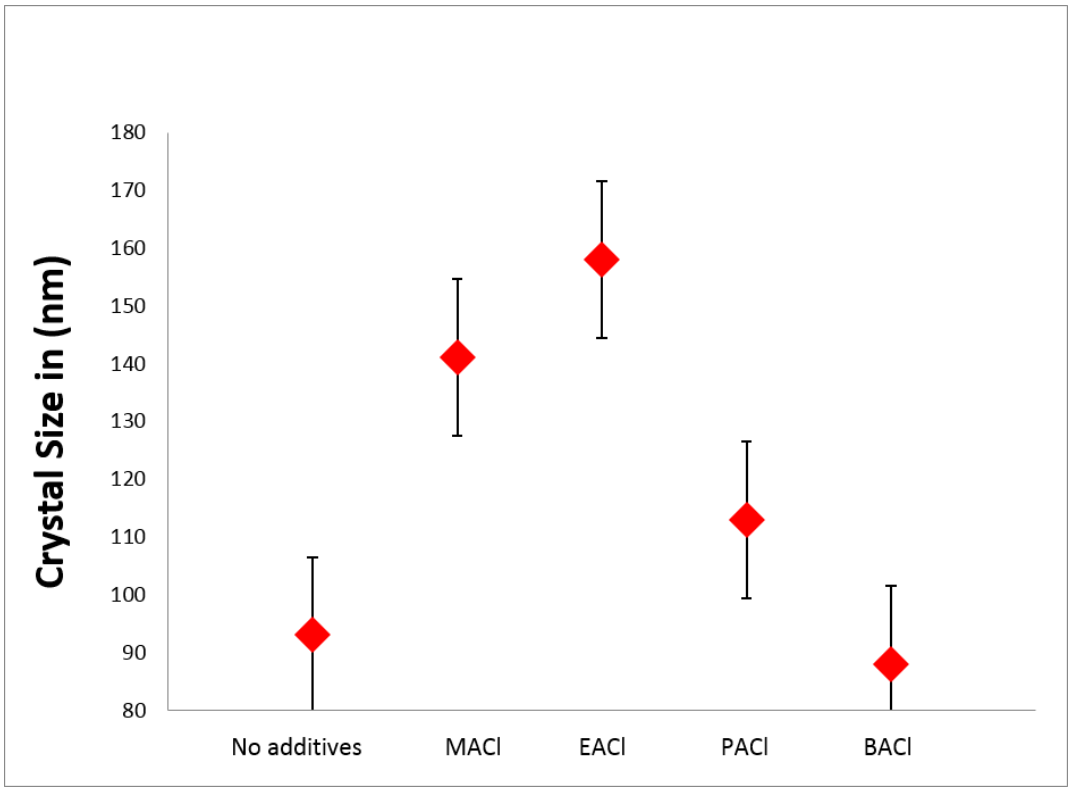

Figure 1. Grain size comparison for different chloride precursors in lead based perovskites

The effect of different chloride based precursors with different alkyl chain length was also studied. We replaced the different anions instead of Cl^- ion in the optimized chloride precursor ethyl ammonium chloride EACl to study their impact on the perovskite crystals. We focused on growing the bigger defect free perovskite crystals using different chloride precursors. We quantitatively measured the crystal size of perovskite crystallites using XRD by Scherrer formula with the FWHM of the peak. The abbreviated forms for different additives we used are as follows CH_3NH_3Cl (MACl), $CH_3CH_2NH_3Cl$ (EACl), $CH_3CH_2CH_2NH_3Cl$ (PACl), and $CH_3CH_2CH_2CH_2NH_3Cl$ (BACl). We achieved maximum crystal size of 158 nm with EACl as additive as shown in the figure 1. Other important parameters such as micro strain in the crystal lattice, and dislocation density was also calculated for the perovskite films. Formation of bigger crystals and high surface area coverage of perovskites are also studied by field emission scanning electron microscopy (FE-SEM). Optical bandgap of the materials was found using photoacoustic spectra. Defects in the perovskite crystals was studied using the calculated Urbach energy.

After the optimization of EACl the best additive we employed EACl in the two step methodology with different solvents like DMF and DMSO. The motive of the work was to grow not only the bigger crystals but also with the smooth surface. We characterized the obtained film using XRD, FE-SEM, and surface roughness using AFM. We obtained the grain size of 114 nm with minimum RMS (roughness) value of 72 nm for 100 wt% of EACl as additive with DMSO as the solvent in two step method.

3.2 Experimental

3.2.1 Perovskite film formation (One step method)

One step methodology was chosen for the preparation of all the samples. Slide glasses was used for the preparation of all the samples and sonication was done with deionized water, acetone, and isopropanol for 15 minutes each. Finally UV-ozone (Filgen, Ozone killer, UV-253) treatment were given for 20 min. The mesoporous TiO_2 layer was formed on the glass substrate by diluting dyesol paste PST-30NRD with ethanol in the ratio of 1:5. Mesoporous TiO_2 layer was coated by spin coating at 5000 rpm for 30 s. After that the sample was annealed at 500°C for 30 min. Methyl ammonium iodide and lead iodide was synthesized as demonstrated elsewhere [29]. 1 M of

CH_3NH_3I (MAI) and PbI_2 was dissolved in 1 ml of dimethylformamide (DMF) with different amount of $CH_3CH_2NH_3Cl$ (EACl) to form the perovskite precursor solution. After that solution was sonicated until the precursors was dissolved completely to get the clear solution. The samples without any additives were named as EC0. We added 4 wt%, 8 wt%, and 12 wt% of EACl as the additive which will be called as EC1, EC2, and EC3 respectively. In similar manner other chloride precursors were also added with 1 M of MAI and 1 M of PbI_2 in DMF to form other perovskite films with selected additives. They are abbreviated as follows CH_3NH_3Cl (MACl): MC3, $CH_3CH_2CH_2NH_3Cl$ (PACl): PC3, and $CH_3CH_2CH_2CH_2NH_3Cl$ (BACl): BC3. All the chemicals were bought from sigma-Aldrich and used without further purification. Perovskite layer were formed on to the mesoporous TiO_2 layer by spin coating at 2500 rpm for 30 s and post heated at 110°C for 45 min in an open atmosphere. 12 wt% of $CH_3CH_2NH_3Br$ (EABr) and $CH_3CH_2NH_3I$ (EAI) were also added as the additive for comparative study of different halogen elements $CH_3CH_2NH_3X$. The samples with EABr and EAI as additive was labelled as EB3 and EI3 respectively.

3.2.1.1 Two-step method with DMF and DMSO

In the preparation of perovskite samples in two-step method with EACl as additive same procedure was followed for cleaning the samples. Similarly same process was continued for forming the mesoporous TiO_2 layer. Then 1 M of PbI_2 was taken in DMF or DMSO and the solution was stirred well at 70°C until getting the clear solution. Then solution was spin coated above the mesoporous TiO_2 at 5000 rpm for 10 seconds and post annealed at 75°C for 15 minutes. MAI was taken at weight percentage of 10 mg/ml of isopropanol (IPA) and totally the solution of 40 ml was made. After post annealing of PbI_2 films, they are dipped in the prepared MAI solution for around 2 minutes and clear color change in the film from yellow to black was observed. Finally the obtained films were post annealed at 75°C for 45 minutes after dipping in the MAI solution. In case preparing the films with additive, EACl of different weight percentage like 0%, 20%, 50%, and 100% were added in the IPA solution along with MAI. For the samples we used DMF as the solvent for making PbI_2 was named as DF0, DF1, DF2, and DF3. While for the PbI_2 made with DMSO was named as DO0, DO1, DO2 and DO3 respectively.

3.2.2 Crystallographic studies

XRD patterns for sulfur doped MBI were studied using X-ray diffractometer RINT-Ultima III, Rigaku, Japan employing Cu Ka1 radiation (k = 1.5406 Å). Diffracted rays were registered for every 0.02° of Bragg angle from 10° to 60°. Before the measurement of sample standard silicon samples was measured for calibrating and X-ray intensity for TiO_2/glass was also checked.

3.2.3 Surface morphology studies

Surface morphology of the samples was studied through FE-SEM (Hitachi, S-5200). The samples were cut down to the dimension of 4 mm × 2 mm and platinum was coated above the surface to increase the conductivity. Surface roughness was measured using AFM model JSPM 5200.

3.2.4 Optical absorption studies

Gas-microphone photoacoustic (PA) technique was used for studying the optical absorption properties. At room temperature in the wavelength range of 500-1200 nm with a modulation frequency of 33 Hz. First the microphone output was passed through a preamplifier and a lock-in amplifier before the measurement of PA signal. Carbon black sheet's spectrum were used for normalizing the obtained PA spectra.

3.3 Results & Discussion

3.3.1 Ethyl ammonium chloride (EACl) as additive

Figure 2 shows the XRD patterns for different perovskite samples EC0, EC1, EC2 and EC3 with EACl as additive in different ratios. Our XRD reports were in good agreement with the literature.[18] The obtained perovskite crystals are polycrystalline in nature with tetragonal phase [17] and have preferred orientation along (110) and (220) plane. No additional peaks were found other than the related peaks to $MAPbI_3$. Also no corresponding peaks were found for $MAPbCl_3$ or $PbCl_2$ which was similar to the literature for other chloride precursor's.[26-28] The grain size of the perovskite crystals was calculated using the standard Scherrer formula.[29] In order to make the grain size precise instrumental parameters for all the samples were kept fixed. Addition of EACl made a drastic increase in the grain size of the perovskite crystals. The grain size of the perovskite crystals was increased in proportion to the wt% of EACl as given in Table 1, while the samples with no additives have the grain size of 93 nm which was increased maximum of 158 nm

for EC3 sample with 12 wt% of EACl. Ostwald ripening phenomenon could be chargeable for the increase in crystal size due to the incorporation of Cl^- ion. [23]

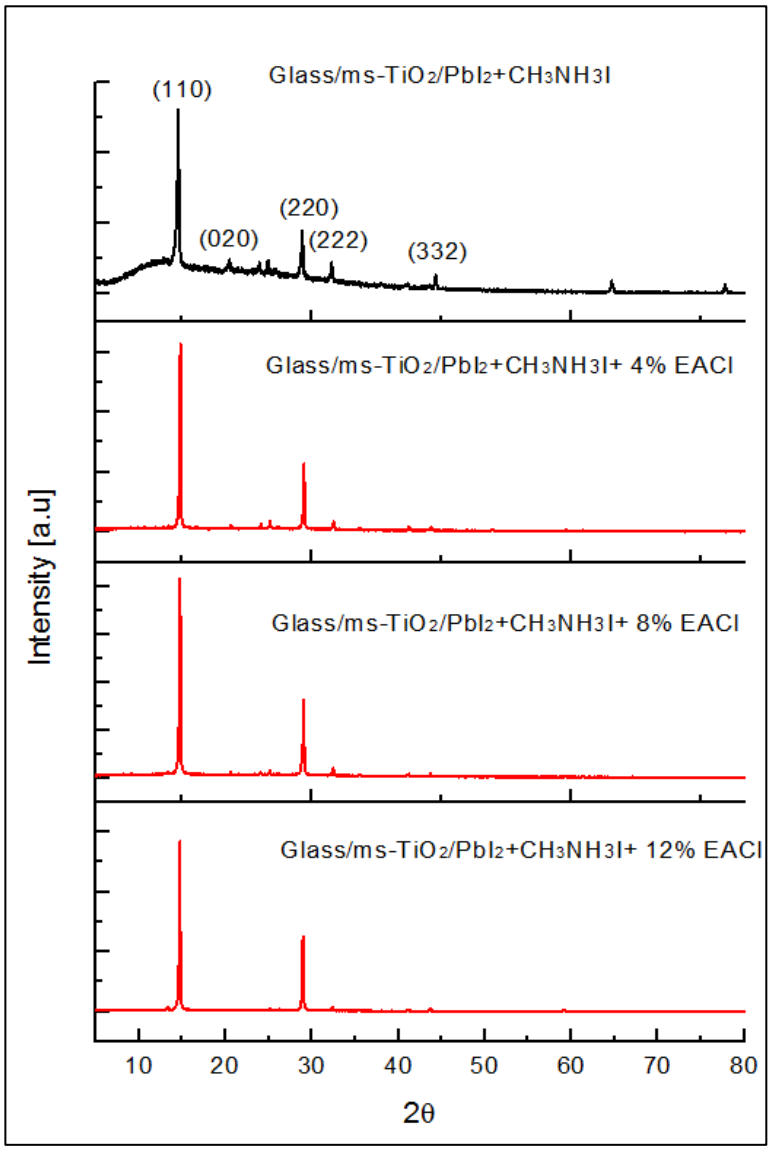

Figure 2. XRD Patterns for the perovskite film with no additive and EACl as additive in different wt % (a) sample EC0 (b) sample EC1 (c) sample EC2 (d) sample EC3

Crystallinity of the samples was also enhanced highly by the addition of EACl as we can see from Figure 2 the orientation along (020), (220), (222) and (332) planes was relatively decreasing as the EACl concentration increases. In that sample EC3 has almost preferred orientation only along

(110) and (220) plane. Increase in the intensity towards the preferred orientation was also noted corresponding to the wt% of EACl which clearly shows that the addition of EACl highly enhances the quality of perovskite crystals.

Table 1. Calculated XRD parameters of the samples with different amount of EACl

Sample name	Amount of EACl in wt%	Grain Size (nm)	Dislocation density(δ) $\times 10^{13}$ (Line/m^2)	Lattice strain(Ɛ) $\times 10^{-4}$ (Line^{-2}m^{-4})
EC0	0	93	11.5	9.81
EC1	4	132	5.74	6.87
EC2	8	144	4.82	6.31
EC3	12	158	3.98	5.75

In our case we found the size and crystallization of the perovskite crystals varied with different chloride precursors and we finally found that EACl is the better chloride precursor for the perovskite crystal growth. Finally we found that dissociation of Cl^- ions from the particular precursor plays the fundamental role in deciding or controlling the crystallization of perovskite.

Lowest lattice strain obtained for the sample with 12 wt% of EACl may be due to the enhanced crystallization(less vacancy sites) of perovskite crystals. Dislocation density is also very minimum for the sample EC3 which qualitatively reveals that crystallographic defects are reduced due to the addition of EACl. Finally we also increased the amount of EACl up to 20 wt% but there was no considerable change in the XRD pattern and FWHM.

To confirm the formation of bigger crystals field emission scanning electron microscopy (FE-SEM) was used. Figure 3 shows both higher and lower resolution image for the samples EC0 and EC3. Both higher and lower magnification images(c, d, e) of sample EC3 shows the more surface area coverage of perovskite on the porous TiO_2 layer when compared to the images (a, b, c) of sample EC0 in which the bare TiO_2 can be seen in between the perovskite crystals. The increase in the density of perovskite crystals may due to the larger grain size and better crystallinity enhanced by the chloride ions in EACl. The higher magnification image (f) of sample EC3 clearly shows the formation of larger crystals when compared to sample EC0 which matches with our XRD data. Crystal agglomeration is clearly seen in the sample EC3, which may be the reason for

the increase in the density of perovskite crystals and for the larger grain size obtained from the XRD results.

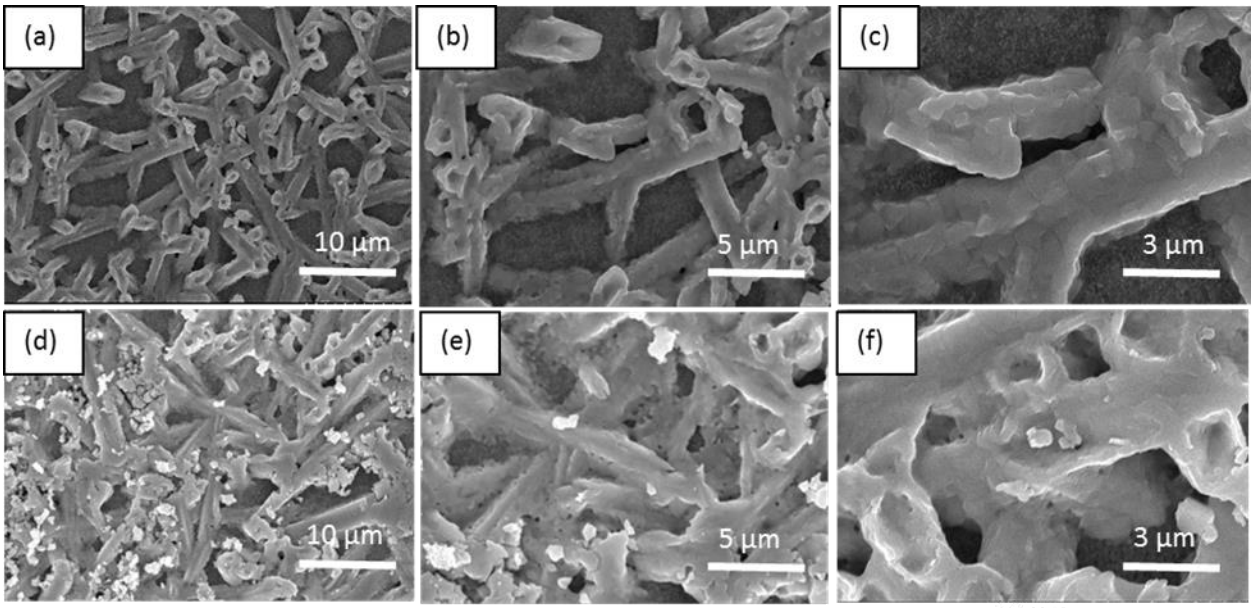

Figure 3. FE-SEM images of $MAPbI_3$ with and without additives. (a-c) Sample EC0 without any additives. (d-f) Sample EC3 with 12 wt% of EACl.

3.3.2 Relationship between alkyl chain length and grain size

In order to know the perfect chloride precursor for ameliorating the perovskite crystal we tried with different chloride precursors like MACl, EACl, PACl, and BACl at different ratios. Figure 4 shows the obtained XRD patterns for the samples MC3, EC3, PC3, and BC3. But we found the maximum grain size and better crystallinity only for the samples which has the additives at the quantity of 12 wt%. We found that the grain size of the perovskite crystals are highly affected by the length of alkyl chain in chloride precursors as shown in Table 2. It could be attributed to the variation in the dissociation of Cl^- ions from the different chloride precursors as discussed earlier.

Dissociation of the chloride ions, therefore, plays the vital role in controlling the parameters during growth of the perovskite crystals. Although addition of MACl increased the crystal size up to 78 nm, crystallinity was poor as can be seen due to the appearance of the additional peaks other than (110) and (220) [26]. Interestingly, in the case of EACl as additive, it not only increases the grain size but also led to the enhanced crystal quality. Eventually the addition of chloride

precursors with longer alkyl chains rapidly decreased the grain size of the perovskite crystals to the extreme of 53 nm for 12 wt% of BACl. This decrease in the grain size may be due to the variation in the decomposition rate of the additives. The grain size of different precursors was increasing in the order of EACl > MACl > PACl > BACl. Although exact mechanism is not yet completely clear but it could be attributed to the variable decomposition and loss of the byproducts of additives specially shown by equation 2b which has also been proposed by Williams et al. [24] for the loss of chloride.

$$Cl^- + R\text{-}NH_3^+ \leftrightarrow R\text{-}Cl\ (s) \quad (1)$$

$$R\text{-}Cl\ (s) \leftrightarrow R\text{-}Cl\ (g) \quad (2a)$$

$$R\text{-}Cl\ (s) \leftrightarrow HCl + R\text{-}NH_2 \quad (2b)$$

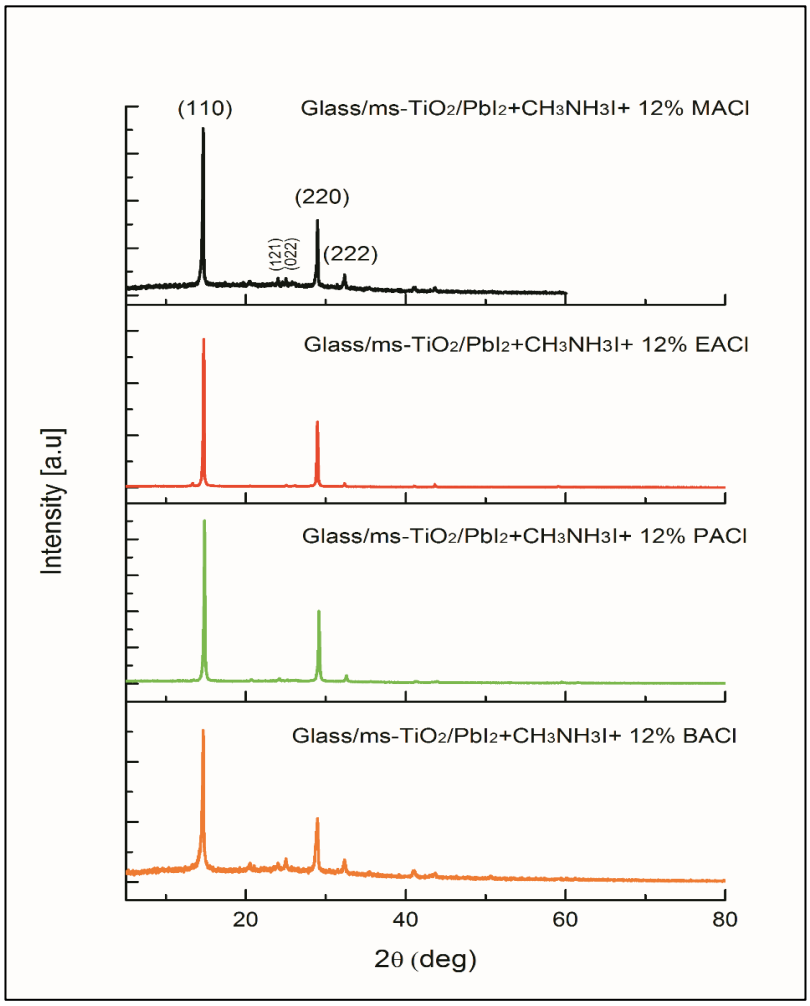

Figure 4. XRD Patterns for the perovskite film with different alkyl chain length chloride precursors (a) sample MC3 (b) sample EC3 (c) sample PC3 (d) sample BC3

In the above equations (1-2b) R represents CH_3, CH_3CH_2, $CH_3CH_2CH_2$, and $CH_3CH_2CH_2CH_2$. It can be clearly seen that final alkylamine byproduct dictates the loss of chloride ion during the formation of active perovskite layer. Boiling points of corresponding alkylamines also varies in the order of CH_3-NH_2 (-6^{o}C) < CH_3-CH_2-NH_2 (17^{o}C) <CH_3-CH_2-CH_2-NH_2 (48^{o}C) <CH_3-CH_2-CH_2-CH_2-NH_2 (78^{o}C). Due to very low boiling point of methylamine in the case MACl, there is uncontrolled release of amine and HCl byproducts during post heating which is relatively controlled for EACl. Since the boiling point of propyl and butyl amines are higher than ethylamine, their removal might be hindered especially the species trapped in the interstitial spaces and could be responsible for lower grain size.

Table 2. Calculated XRD parameters of the samples with different alkyl chain length chloride precursors

Sample name	Different chloride precursors at 12 wt%	Grain Size (nm)	Dislocation density(δ) $\times 10^{13}$ (Line/m^2)	Lattice strain(Ɛ) $\times 10^{-4}$ (Line^{-2}m^{-4})
MC3	MACl	122	6.73	7.51
EC3	EACl	158	3.98	5.75
PC3	PACl	113	7.81	7.9
BC3	BACl	105	9.2	8.67

3.3.3 Effect of different anion in the additive $CH_3CH_2NH_3X$

XRD patterns with different anions in $CH_3CH_2NH_3X$ was given in Figure 5. The grain size of perovskite was decreased when Cl^- ions are replaced with different anions like Br^- and I^- as showed in the Table 3. Also the crystallinity of the samples was very poor. After comparing the grain size and crystallinity of the samples we can come to a conclusion that the dissociation of Cl^- ions really plays vital role in the fixing the grain size and crystallinity of perovskite crystals.

Table 3. Calculated XRD parameters of the samples with different halogen element in $CH_3CH_2NH_3X$

Sample name	$CH_3CH_2NH_3X$ with different X at 12 wt%	Grain size (nm)	Dislocation density(δ) $\times 10^{13}$ (Line/m^2)	Lattice strain(Ɛ) $\times 10^{-4}$ (Line^{-2}m^{-4})
EC3	Cl	158	3.98	5.75
EB3	Br	113	7.81	8.05
EI3	I	72	19.3	12.63

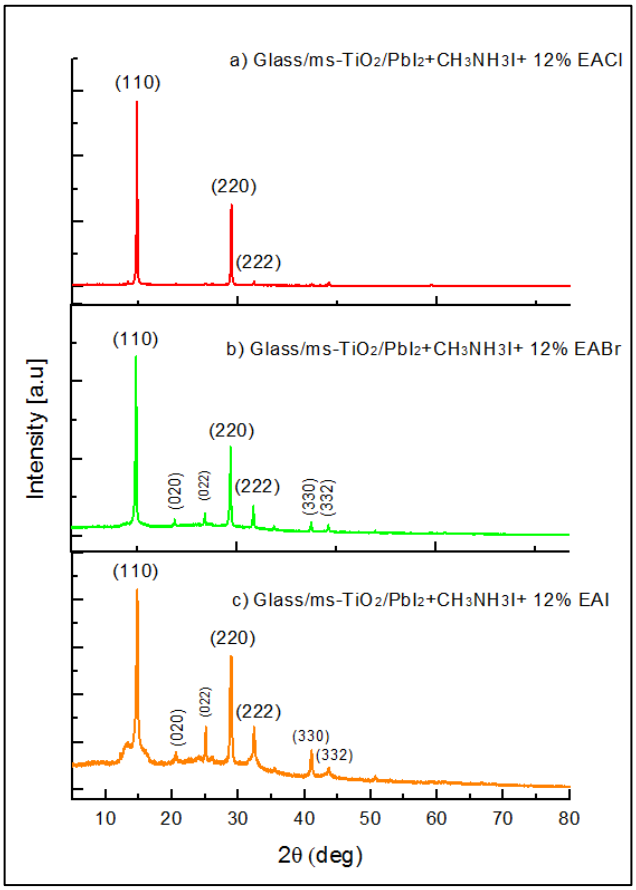

Figure 5. XRD Patterns for the perovskite film with different halogen element in $CH_3CH_2NH_3X$ (a) sample EC3 (b) sample EC3 (X= Cl) (c) sample EB3 (X= Br) (d) sample EI3 (X=I).

3.3.4 Photoacoustic studies

Using Photoacoustic spectral measurements, the intensities of the PA (Photoacoustic) signals are plotted semi logarithmically which varied linearly below the absorption edges for different ratios of EACl in accordance with the Urbach rule for the optical absorption coefficient as shown in the Figure 6. Optical bandgap of all the prepared samples were found to be 1.54 eV and no shift in bandgap was observed by the addition of EACl. An empirical relationship for the dependence of PA signal intensity P on measuring temperature (T) and photon energy (hυ) was fitted by equation 3.

$$P = P_0 \exp[\sigma(h\upsilon - h\upsilon_0)/kT] \quad (3)$$

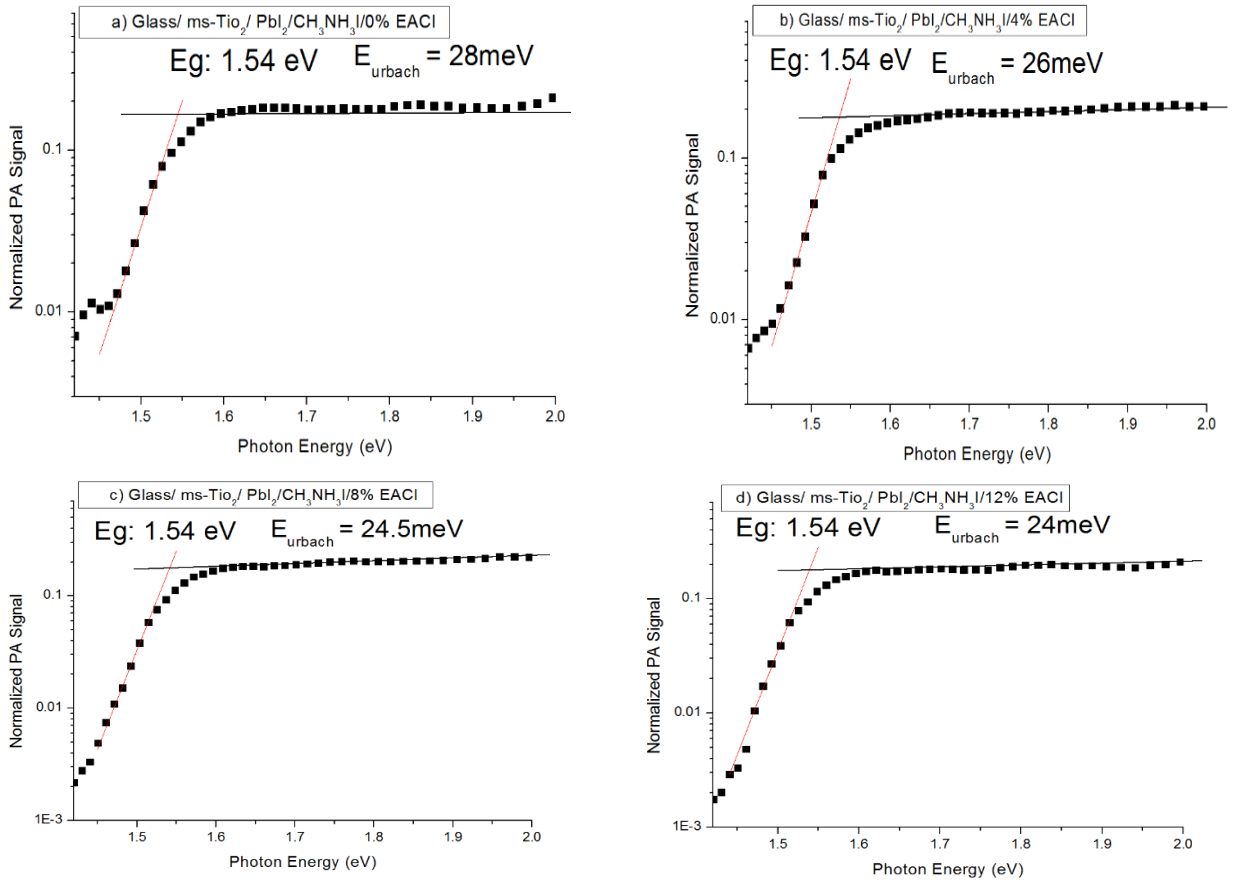

Figure 6. Optical absorption spectrum of $MAPbI_3$ with and without additives measured using photoacoustic (PA) technique. (a) Sample EC0 (b) sample EC1 (c) sample EC2 (d) sample EC3

Where, *k* is Boltzmann constant, and P_0, σ and υ_0 are fitting parameters [30] while σ is the steepness factor and was determined from the slope of the exponential optical absorption. The relation *k*T/σ, which is the width of the exponential tail, is called the Urbach energy UE. Because of the nature of the temperature dependence of the Urbach tail α has the exponential behavior due to the interaction of electrons and excitons with phonons. The calculated steepness factor for our samples was increased as the concentration of EACl increases as shown in Table 4. Even though increase in σ represents various phenomena [31] in our case it highlights the surface states on nanocrystals. It may be on the behalf of decrease in the electronic density states with respect to surface state density due to increase in the crystal size of the perovskites. Higher uniformity among the perovskite crystals also may be responsible for the increase in steepness factor. Figure 6 shows the plot between the steepness factor and different wt% of EACl additives. Urbach energy (UE) [32-33] is basically the quantitative representation of the slope in that exponential trend below the optical bandgap. Interestingly in our samples, UE was found to decrease as a function of the EACl concentration of as shown in the Table 4. Information on the band structure, disorder, defects, impurities and electron–phonon interactions in semiconductor materials could be studied by comparing this UE [32-33]. Therefore, decreased UE for the EC3 indicates that the addition of EACl as additive decreases the crystal disorder in the perovskite crystals leading to reduced recombination, which highly essential for the perovskite solar cells. Figure 7 shows the plot between the steepness factor and different wt % of EACl.

Table 4. Calculated Urbach energy and Steepness factor of the samples with different amount of EACl

Sample name	Amount of EACl in wt%	Bandgap Energy E_g	Urbach Energy E_{Urbach}	Steepness Factor
EC0	0	1.54 eV	28 meV	0.89
EC1	4	1.54 eV	26 meV	0.96
EC2	8	1.54 eV	24.5 meV	1.02
EC3	12	1.54 eV	24 meV	1.04

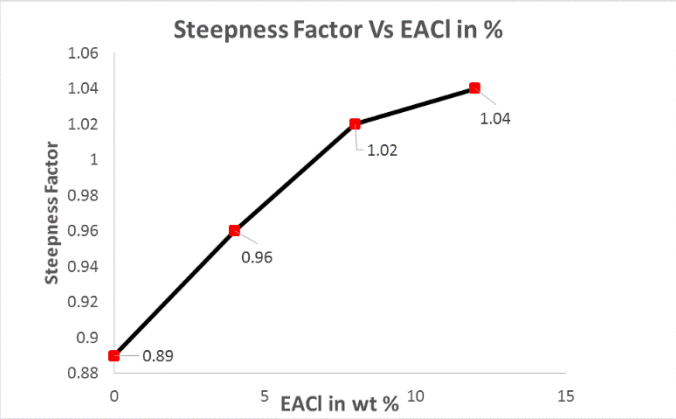

Figure 7. Steepness Factor Vs EACl in %

3.3.5 Ethyl ammonium chloride as the additive in two-step method

3.3.5.1 DMF as solvent

After the finding the suitable chloride precursor as EACl for lead based perovskites, we employed the EACl additive in two-step methodology for making perovskite layer. EACl of different weight percentage like 0%, 20%, 50%, and 100% were taken and the samples we used DMF as the solvent for making PbI_2 was named as DF0, DF1, DF2, and DF3. Figure 8 shows the XRD obtained for the different samples with EACl as additive. No additional peaks or peaks related $MAPbCl_3$ were found in the XRD pattern. Grain size rapidly increased from 68 nm (0 wt% EACl) to 120 nm (20 wt%) which is almost double. The grain size further increased up to 123 nm for 50 wt% of EACl and decreased to 121 nm for 100 wt% of EACl. From the AFM measurement surface roughness was measured using root mean square (RMS) value R_q. The surface of samples were found to be very rough as shown in figure 9. The roughness for the sample without additive is 235 nm while with 100 wt% of EACl the roughness was decreased to 155 nm. Even though there is decrease in the roughness values comparatively, the values obtained was too high and may result in poor device performance. So, we planned to do the same experiment with DMSO as the solvent. Because in two-step method the crystallinity of the perovskite samples mainly depends on the crystal quality and morphology of the PbI_2. We selected DMSO as the alternative since the boiling point of DMSO (189°C) is lower than that of DMF (153°C) which will be helpful in the slow

crystallization of PbI_2 and high probability for better perovskite surface. Table 5 shows the XRD parameters and roughness (RMS) values obtained for the samples.

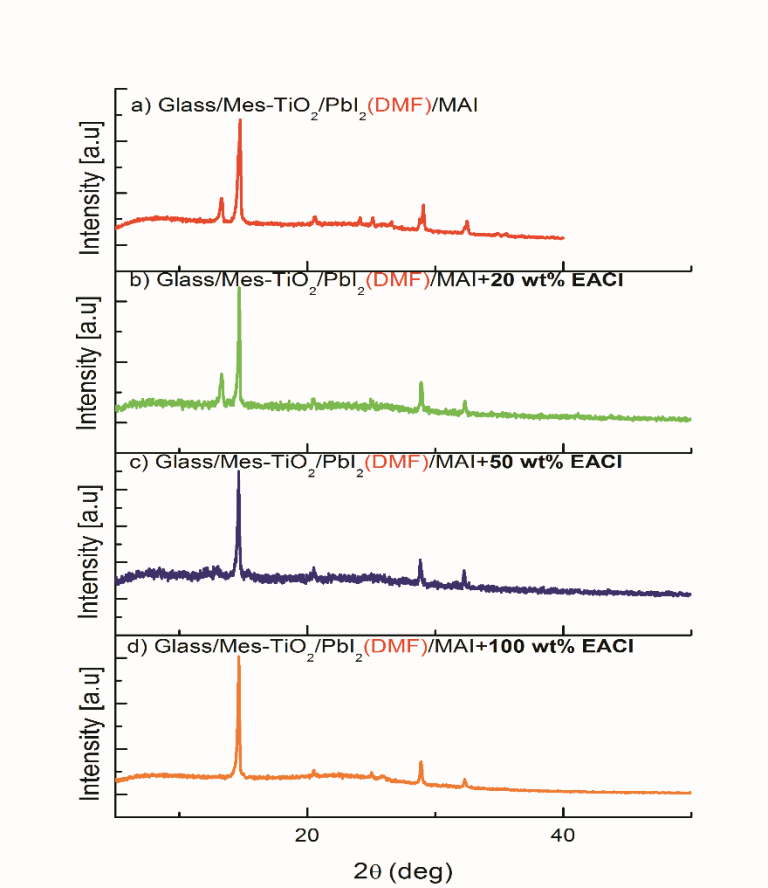

Figure 8. XRD Patterns for the perovskite film with EACl as additive (a) sample DF0 (b) sample DF1 (c) sample DF2 (d) sample DF3.

a) No Additive **b) 20 wt% EACl** **c) 50 wt% EACl**

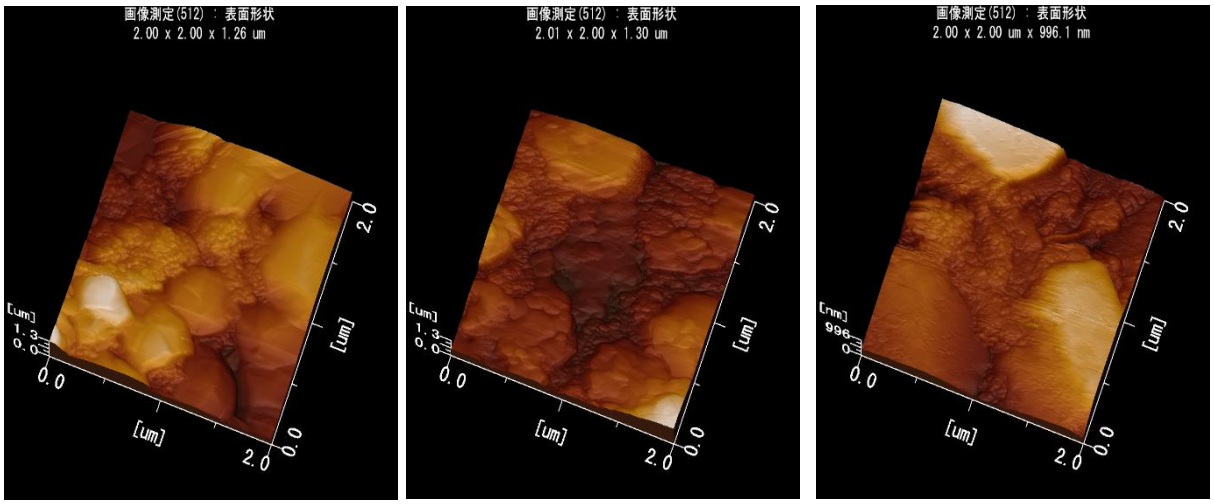

d)100 wt% EACl

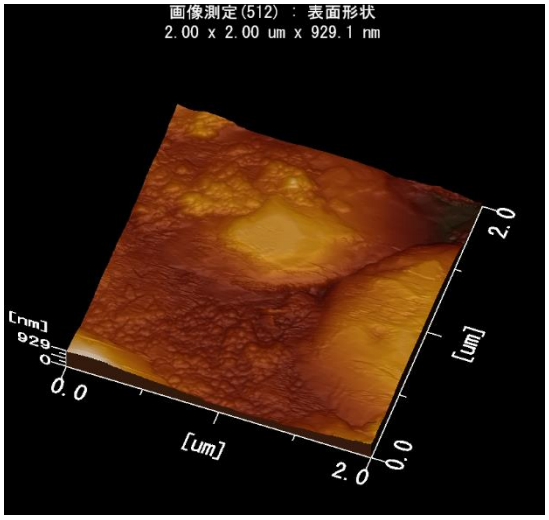

Figure 9. AFM images for the perovskite film with EACl as additive (a) sample DF0 (b) sample DF1 (c) sample DF2 (d) sample DF3.

Table 5. Calculated XRD parameters and roughness (RMS) values of the samples with EACl as additive in two-step method (DMF)

Amount of EACl in wt%	Grain Size (nm)	RMS (Roughness) in nm
0	68	235
20	120	229
50	123	190
100	121	155

3.3.5.2 DMSO as solvent

The crystallization process of PbI_2 with DMSO was found to be very slow as compared to DMF due the high boiling point as we mentioned earlier. After the PbI_2 solution was spin coated very slow change in color was observed. EACl of different weight percentage like 0%, 20%, 50%,

and 100% were taken and the samples we used DMSO as the solvent for making PbI_2 was named as DO0, DO1, DO2 and DO3 respectively. The XRD patterns obtained for the above samples are

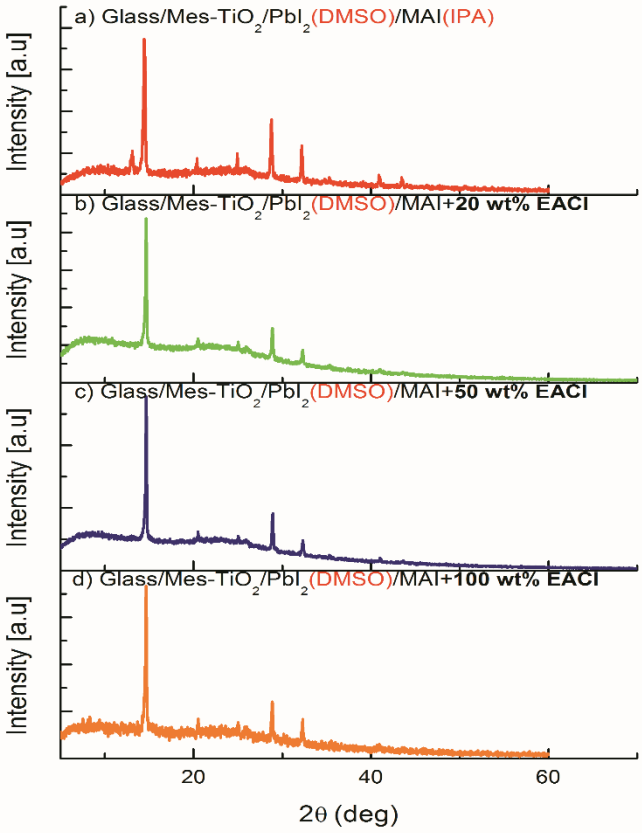

Figure 10. XRD Patterns for the perovskite film with EACl as additive (a) sample DO0 (b) sample DO1 (c) sample DO2 (d) sample DO3.

shown in the figure 10. Similar to DMF in the case of DMSO also no additional or impure peaks were found in the XRD. The trend of increase in grain size was similar to that of DMF as shown in the Table 6. From the FE-SEM cuboid morphology was obtained as shown in the figure 11. Bigger crystals were apparently found from the FE-SEM images as the concentration of EACl was increased. However, for the higher concentration of EACl above 50 wt% the crystals started to agglomerate with smooth and complete surface area coverage. From measured AFM images the roughness of the samples were reduced rapidly in comparison with DMF as clearly seen from the figure 12. Minimum roughness of 72 nm was obtained for 100 wt% of EACl while the minimum roughness obtained with DMF was 155 nm. Detailed comparison of both grain size and roughness for both the solvents DMF and DMSO was given in figure 13.

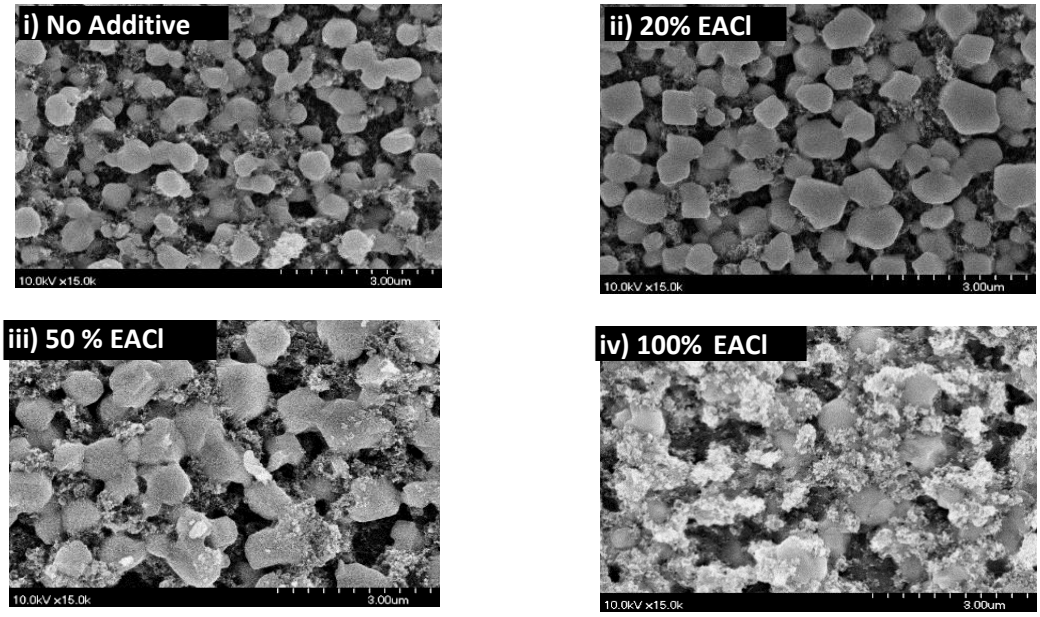

Figure 11. FE-SEM images for the perovskite film with EACl as additive (i) sample DO0 (ii) sample DO1 (iii) sample DO2 (iv) sample DO3.

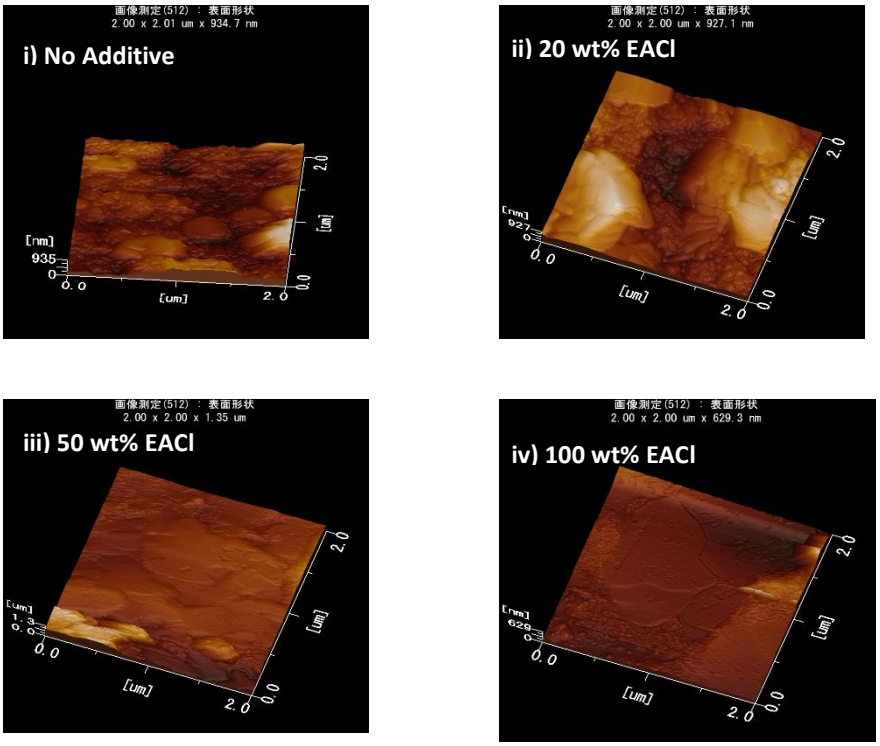

Figure 12. AFM images for the perovskite film with EACl as additive (i) sample DO0 (ii) sample DO1 (iii) sample DO2 (iv) sample DO3.

Table 6. Calculated XRD parameters and roughness (RMS) values of the samples with EACl as additive in two-step method (DMSO)

Amount of EACl in wt%	Grain Size (nm)	RMS (Roughness) in nm
0	65	165
20	118	199
50	133	178
100	114	72

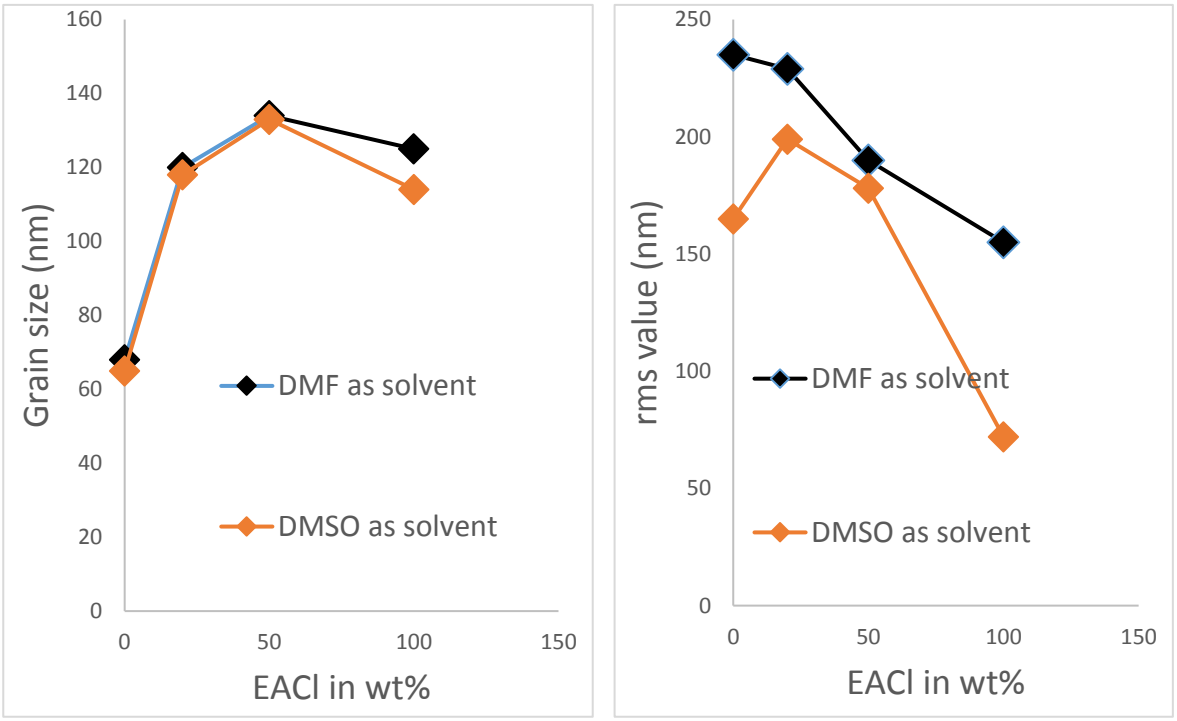

Figure 13. Detailed comparison of both grain size and roughness for both the solvents DMF and DMSO

3.4 Conclusions

Finally the crystallization process of the perovskite film by adding different types of chloride additives was investigated. The perfect chloride precursor and its quantity was successfully found. XRD results shows that the bigger crystals were formed by the addition of EACl at 12 wt% when compared to other chloride based additives. Other crystalline parameters such as dislocation density, and lattice strain were also studied. We also compared the effect of alkyl chain length in different chloride precursors in the crystallization process. From our studies huge impact in dissociation of Cl^- ions towards the crystallization of perovskite crystals was confirmed. FE-SEM images apparently shows the better crystallinity and surface coverage of our samples. Photoacoustic studies ensures the addition of EACl has enhanced the crystallinity, and also reduced the crystal defects in the perovskite layer without any modification in the optical bandgap. All these findings says that for one step preparation method EACl at 12 wt% is the suitable chloride precursor in order to control the growth of perovskite crystals with lower defects. We also optimized the EACl precursor in two step methodology with different solvents like DMF and DMSO. In case of both the solvents grain size was increasing, but rough surface was obtained for DMF. However, for DMSO we obtained the smooth surface with bigger crystal size due to its high boiling point.

3.5 References

1) Eperon, Giles E. "Formamidinium lead trihalide: a broadly tunable perovskite for efficient planar heterojunction solar cells." *Energy & Environmental Science* 7.3 (2014): 982-988.
2) Kojima, Akihiro, "Organometal halide perovskites as visible-light sensitizers for photovoltaic cells." *Journal of the American Chemical Society*131.17 (2009): 6050-6051.
3) Pedesseau, Laurent, "Electronic properties of 2D and 3D hybrid organic/inorganic perovskites for optoelectronic and photovoltaic applications."*Optical and Quantum Electronics* 46.10 (2014): 1225-1232.
4) Luo, Jingshan, "Water photolysis at 12.3% efficiency via perovskite photovoltaics and Earth-abundant catalysts." *Science* 345.6204 (2014): 1593-1596.
5) http://www.nrel.gov/ncpv/.
6) Zhou, Huanping, "Interface engineering of highly efficient perovskite solar cells." *Science* 345.6196 (2014): 542-546.
7) Koh, Teck Ming, "Formamidinium-containing metal-halide: an alternative material for near-IR absorption perovskite solar cells." *The Journal of Physical Chemistry C* 118.30 (2013): 16458-16462.
8) Xiao, Zhengguo, "Efficient, high yield perovskite photovoltaic devices grown by interdiffusion of solution-processed precursor stacking layers."*Energy & Environmental Science* 7.8 (2014): 2619-2623.
9) Jeon, Nam Joong, "o-Methoxy substituents in Spiro-OMeTAD for efficient inorganic–organic hybrid perovskite solar cells." *Journal of the American Chemical Society* 136.22 (2014): 7837-7840.
10) Conings, Bert, "Perovskite-Based Hybrid Solar Cells Exceeding 10% Efficiency with High Reproducibility Using a Thin Film Sandwich Approach."*Advanced Materials* 26.13 (2014): 2041-2046.
11) Jeng, Jun-Yuan, "$CH_3NH_3PbI_3$ Perovskite/Fullerene Planar-Heterojunction Hybrid Solar Cells." *Advanced Materials* 25.27 (2013): 3727-3732.
12) Im, Jeong-Hyeok, "Growth of $CH_3NH_3PbI_3$ cuboids with controlled size for high-efficiency perovskite solar cells." *Nature nanotechnology* 9.11 (2014): 927-932.

13) Abrusci, Agnese, "High-performance perovskite-polymer hybrid solar cells via electronic coupling with fullerene monolayers." *Nano letters* 13.7 (2013): 3124-3128.

14) Ball, James M., "Low-temperature processed meso-superstructured to thin-film perovskite solar cells." *Energy & Environmental Science* 6.6 (2013): 1739-1743.

15) Liang, Po-Wei, "Additive enhanced crystallization of solution-processed perovskite for highly efficient planar-heterojunction solar cells." *Advanced Materials* 26.22 (2014): 3748-3754.

16) Jeon, Nam Joong, "Solvent engineering for high-performance inorganic–organic hybrid perovskite solar cells." *Nature materials* (2014).

17) Park, Byung-wook, "Enhanced Crystallinity in Organic–Inorganic Lead Halide Perovskites on Mesoporous TiO_2 via Disorder–Order Phase Transition."*Chemistry of Materials* 26.15 (2014): 4466-4471.

18) Colella, Silvia, "$MAPbI_{3-x}Cl_x$ Mixed Halide Perovskite for Hybrid Solar Cells: The Role of Chloride as Dopant on the Transport and Structural Properties." *Chemistry of Materials* 25.22 (2013): 4613-4618.

19) Kim, Hui-Seon, and Nam-Gyu Park. "Parameters affecting I–V hysteresis of CH3NH3PbI3 perovskite solar cells: effects of perovskite crystal size and mesoporous TiO2 layer." *The Journal of Physical Chemistry Letters* 5.17 (2014): 2927-2934.

20) Docampo, Pablo, "Solution Deposition-Conversion for Planar Heterojunction Mixed Halide Perovskite Solar Cells." *Advanced Energy Materials* 4.14 (2014).

21) Wehrenfennig, Christian, "Homogeneous Emission Line Broadening in the Organo Lead Halide Perovskite $CH_3NH_3PbI_{3-x}Cl_x$." *The Journal of Physical Chemistry Letters* 5.8 (2014): 1300-1306.

22) Zheng, Fan, "First-Principles Calculation of Bulk Photovoltaic Effect in $CH_3NH_3PbI_3$ and $CH_3NH_3PbI_{3-x}Cl_x$." *The Journal of Physical Chemistry Letters* (2014).

23) Dar, M. Ibrahim, "Investigation regarding the role of chloride in organic–inorganic halide perovskites obtained from chloride containing precursors."*Nano letters* 14.12 (2014): 6991-6996.

24) Williams, Spencer T., "Role of chloride in the morphological evolution of organo-lead halide perovskite thin films." *ACS nano* 8.10 (2014): 10640-10654.

25) Wang, Dong, "Reproducible One-Step Fabrication of Compact $MAPbI_{3-x}Cl_x$ Thin Films Derived from Mixed-Lead-Halide Precursors." *Chemistry of Materials* 26.24 (2014): 7145-7150.
26) Zhao, Yixin, and Kai Zhu. "$CH_3NH_3Cl^-$Assisted One-Step Solution Growth of $CH_3NH_3PbI_3$: Structure, Charge-Carrier Dynamics, and Photovoltaic Properties of Perovskite Solar Cells." *The Journal of Physical Chemistry C* 118.18 (2014): 9412-9418.
27) Zuo, Chuantian, and Liming Ding. "An 80.11% FF record achieved for perovskite solar cells by using the NH_4Cl additive." *Nanoscale* 6.17 (2014): 9935-9938.
28) Chen, Yani, Yixin Zhao, and Ziqi Liang. "Non-Thermal Annealing Fabrication of Efficient Planar Perovskite Solar Cells with Inclusion of NH_4Cl." *Chemistry of Materials* 27.5 (2015): 1448-1451.
29) Patterson, A. L. "The Scherrer formula for X-ray particle size determination."*Physical review* 56.10 (1939): 978.
30) Shen, Qing, and Taro Toyoda. "Photoacoustic Studies of Annealed CdS_xSe_{1-x} (x= 0.26) Nanocrystals in a Glass Matrix." *Japanese journal of applied physics*38.5S (1999): 3163.
31) Zammit, U., "Optical-absorption studies of ion-implantation damage in Si on sapphire." *Physical Review B* 49.20 (1994): 14322.
32) Urbach, Franz. "The long-wavelength edge of photographic sensitivity and of the electronic absorption of solids." *Physical Review* 92.5 (1953): 1324.
33) Keil, Thomas H. "Theory of the Urbach rule." *Physical Review* 144.2 (1966): 582.

Chapter 4. Sulfur doped low band gap bismuth based perovskites for solar cells application

4.1 Introduction

Low cost, air-stable and ecofriendly functional materials are highly required for the large scale production of next generation solar cells. Recent past has witnessed the emergence of lead halide perovskites $MAPbX_3$ (MA = CH_3NH_3, X = I, Cl, Br) as potential candidate for the next generation solar cells opening the new possibility of low cost production while maintaining the high photo conversion (22.1%).[1] This remarkable enhancement in the photo conversion efficiency could be credited to the fast pace development of efficient hole and electron transporting materials .[2-3] In spite of sky-rocketing success in the lead halide perovskites in such a short-time, currently Pb in this perovskite structure has become the matter of concern owing to its toxicity along with the high susceptibility to moisture. Therefore, it is indispensable to replace the Pb with other metal cations without altering the photovoltaic performance of the material. Owing to diminished toxicity of Sn and Bi along with the matching ionic radius to form perovskite structure they are strong contender to replace the Pb. Recent investigations in this regards towards the replacement of Pb by Sn have raised the serious issue on the environmental stability [4] and reduced photovoltaic performance.[5] These issues have led to the search for other alternate materials and Bi metal has gained a good deal of attention from the material science community. Bismuth based perovskite, methyl ammonium iodobismuthate with molecular formula $CH_3NH_3)_3Bi_2I_9$, (MBI) has been reported to be environment friendly and relatively more stable as compared to the lead halide perovskites. Apart from this, MBI possesses very good semiconducting, electronic, optical and ferroelectric properties along with the rich structural diversity.[6] In MBI, $6s^2$ lone pair from Bi^{3+} plays a crucial role in controlling all the physicochemical properties.[7]

Park et al. [8] have reported Bi based organic-inorganic hybrid perovskites having chemical structure $A_3Bi_2I_9$ (A= CH_3NH_3 or Cs) by replacing Pb with Bi and used as active component for the perovskite solar cells. Unfortunately, large number of defect states and large optical bandgap (about 2.1~2.4 eV) of this material resulted in to very poor photo conversion efficiency. Lyu et al.

[6] have also investigated MBI based solar cells and its fundamental properties, but due to background carrier concentration, low carrier mobility and wide bandgap resulted in to very poor efficiency (0.2 %). Oz et al. [9] have also employed zero-dimensional MBI for photovoltaic application but ended up with negligible efficiency of 0.1 % due to the wide bandgap (2.9 eV). A perusal of these reports clearly corroborates that bandgap tuning of MBI is mandatory in order to realize the improved photovoltaic performance. Therefore, development of Bi based perovskite by replacing Pb with Bi without disturbing the basic properties of lead halide perovskites is highly desired. Main asset of the perovskite structure is that material properties like dimensionality, crystal and electronic structures are tunable.[10] The material property can be altered by changing A, B and X in the chemical structure $A_3B_2X_9$ or by stoichiometry and size of the atoms. [11-12] Towards the development of novel MBI, although efforts have been directed by replacing organic $CH_3NH_3^+$ to inorganic NH_4^+ but measured bandgap was high (2.04 eV).[13] Slavney et al.[14] have also attempted to incorporate Bi_3^+ into the perovskite crystal lattice to form $Cs_2AgBiBr_6$ double perovskite but measured bandgap of the material was still 1.95 eV. A novel perovskite having formula $MABiSI_2$ has been theoretically proposed using split anion approach. Aim of this proposal was to get similar properties that of lead halide perovskite but its experimental verification is yet to be done. [15]

Therefore, narrow bandgap Bi based perovskites are highly desired in order for their successful utilization as active material for the photovoltaic applications. In this work, we have experimentally demonstrated the development of novel sulfur doped MBI on the glass substrates exhibiting a bandgap of 1.45 eV. To prepare this lower bandgap MBI, we have implemented a novel strategy, where $Bi(xt)_3$ (xt = Ethyl xanthate) has been used as the soluble precursor instead of Bi_2S_3 or BiSI in combination with methyl ammonium iodide followed by its thermal annealing.

4.2 Experimental

4.2.1 Synthesis of bismuth (III) ethyl xanthate

Bismuth (III) nitrate pentahydrate (30.9 g, 63.7 mmol) was dissolved in 500 mL of deionized water and 55 mL of hydrochloric acid was added until suspension became clear. A solution of potassium ethyl dithiocarbonate (32.7 g, 204.0 mmol) in 100 mL of deionized water

was added under stirring and a yellow solid was formed immediately. After the reaction solution was stirred for 1 hour, the yellow precipitate was filtered and dried under vacuum. The residue was added in deionized water and dispersed by ultrasonic treatment. After the soluble side products were removed by filtration, the residue was washed thoroughly with deionized water and dried under vacuum.

4.2.2 Making of sulfur doped bismuth perovskite films

For the preparation of sulfur doped MBI, glass substrates were cleaned in the order by distilled water, acetone, and isopropanol for each 15 minutes. Mesoscopic TiO_2 layer was spin coated on the glass substrate by diluting PST-30NRD paste (Dyesol) with ethanol in the ratio of 1: 3 at 5000 rpm for 30 seconds. After that prepared films were annealed at 500^{o}C for 30 minutes. The precursor solution was prepared by mixing $Bi(xt)_3$ and MAI in the molar ratio of 1:2. DMF was used as the solvent and after stirring it continuously for 10 minutes the solution was filtered using 0.45 µm PTFE filter. MBI films was formed by spin coating the precursor solution at 2000 rpm for 15 sec. After spin coating the films was post annealed at different temperatures like 80^{o}C, 120^{o}C, and 150^{o}C.

4.2.2.1 Making of conventional bismuth perovskite film

For the making of conventional bismuth based perovskites the glass samples were cleaned similar to above mentioned process for preparation of sulfur doped MBI. Same kind of procedure for making of mesoporous TiO_2 layer was followed. For making of precursor solution 1 M of BiI_3 and 1 M MAI was taken in 1 ml of DMF and allowed to stir until it made the clear solution. Then solution was spin coated at the speed of 3000 rpm for 30 seconds and post annealed at 120^{o}C for 20 minutes to get the undoped bismuth based perovskites.

4.2.3 Crystallographic and morphology studies

XRD patterns for sulfur doped MBI were studied using X-ray diffractometer RINT-Ultima III, Rigaku, Japan employing Cu Ka1 radiation (k = 1.5406 Å). Diffracted rays were registered for every 0.02° of Bragg angle from 10° to 60°. Before the measurement of sample standard silicon samples was measured for calibrating and X-ray intensity for TiO_2/glass was also checked. Surface morphology of the samples was studied through FE-SEM (Hitachi, S-5200).

4.2.4 Optical absorption and FTIR studies

Jasco V-550 UV–vis spectrophotometer were used for recording the absorption spectra for sulfur doped MBI. Glass coated with mesoporous TiO_2 was used as the reference for the correction of background. Jasco FTIR 4100 was used for the measuring the FTIR spectra for the samples in transmission mode.

4.2.5 Elemental composition studies (XPS)

Wide and high resolution XPS measurements for sulfur doped MBI was performed using Shimadzu/Kratos Axis HSi. AlKα radiation were employed for measuring the samples at the pressure of 1×10^{-6} mbar. Specific core level were repetitively measured in order to minimize the charging and radiation effects.

4.2.6 Thermogravimetric analysis (TGA) and photoelectron yield spectroscopy (PYS)

Thermogravimetric/Differential Thermal Analyzer (TG-DTA) measurements were performed using Shimadzu DTG-60 model. Four milligram of $Bi(xt)_3$ powder was heated at the rate of 20^{o}C/min from ambient temperature to 500^{o}C with nitrogen as purge gas. PYS spectra for the samples were analyzed using PYS, Bunkoukeiki Co., Ltd., BIP-KV201. In preparing samples, sulfur doped MBI was coated over the FTO substrate and post heated at different temperatures.

4.3 Results & Discussion

4.3.1 Reaction scheme

Thermal decomposition of the metal xanthates ultimately leads to metal sulphides via the formation of volatile intermediates like CS_2, COS, CO_2, and CO. [16] Thermal decomposition of $Bi(xt)_3$ finally forms Bi_2S_3 (Scheme-1) having enthalpy of -32.31 ± 0.5 Kcal mole^{-1} at 298 K.[17] At the same time, for the reaction between Bi and I to form BiI3 the enthalpy of formation is -36 ± 1 Kcal mole^{-1} at 298 K [18] which is comparable. Therefore, in the presence of methyl ammonium iodide (MAI), during the decomposition of $Bi(xt)_3$ would most likely tends to form MBI as per the reaction scheme-2. Sulfur generated during the decomposition is expected to dope the MBI thus formed resulting in to the proposed low band gap MBI.

Scheme 1. Decomposition of $Bi(xt)_3$ to Bi_2S_3.

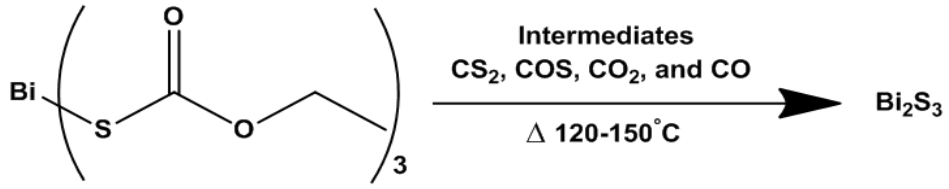

Scheme 2. Decomposition of $Bi(xt)_3$ in the presence of MAI to form sulfur doped MBI.

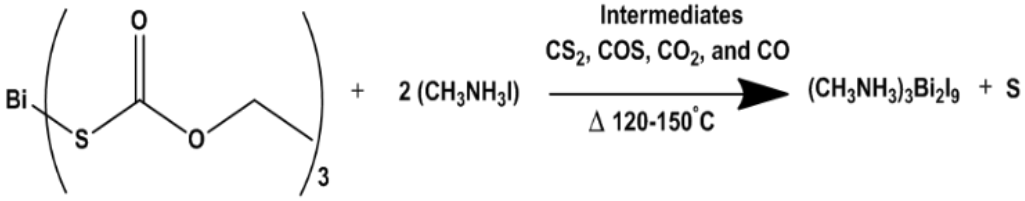

4.3.2 Identification of the material through crystallographic studies (XRD)

XRD patterns of sulfur doped MBI thin films have been shown in the Figure 1. In the crystal structure of MBI metal halide $(Bi_2I_9)^{3-}$ bi-octahedron is separated by MA cation.8 Experimentally obtained XRD patterns are in well agreement with the previously reported XRD patterns of MBI with hexagonal crystal structure and space group as $P6_3/mmc$.[6,19] The obtained lattice parameters of our samples are a = 8.69 Å and c = 21.8 Å and they are comparable with the lattice parameters of MBI single crystals.[20] Cui et al.[21] have reported the bandgap tuning in $MAPbI_3$ by adding Br and demonstrated that addition of Br shifts the 2θ towards the higher value due to the smaller ionic radius of Br (r_{ion} = 1.96 Å) than I(r_{ion} = 2.2 Å) and emphasized the presence of Br in the crystal lattice to form $MAPbBr_xI_{3-x}$. In the present case, neither there was any additional peak nor there was any peak shift in the presence of sulfur compared that of the simulated XRD pattern of the MBI as shown in the Figure 1. This apparently makes us to believe that iodine was not replaced by sulfur and it might be present in the interstitial sites. The samples

post heated at 80°C and other higher temperatures exhibit clear visible color differences as shown in the Figure 1 but in the XRD patterns there was no shift in the 2θ.

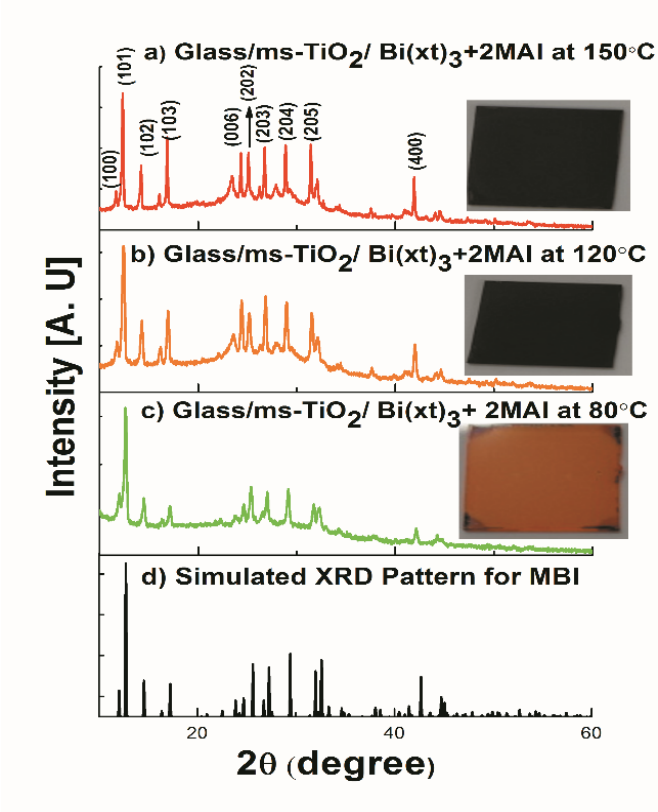

Figure 1. XRD Patterns for sulfur doped MBI at different post heating temperatures (a) 150°C (b) 120°C (c) 80°C and (d) Simulated XRD pattern for undoped MBI

4.3.2.1 Comparative XRD of material with precursors

For finding the impure phases in the Sulfur doped MBI, the obtained XRD pattern of the sulfur doped MBI at 150°C was compared with the precursors methyl ammonium iodide and bismuth ethyl xanthate powder. The XRD pattern of bismuth sulfide powder was also used in the comparison since all the metal xanthates has the tendency to form metal sulfides when they annealed at their particular decomposition temperature. So, bismuth sulfide powder was made by annealing the bismuth ethyl xanthate powder at 150°C in a crucible. After annealing it for over 30 minutes black colored bismuth sulfide powder was subjected for the XRD studies. Figure 2 shows the overall XRD comparison and the obtained patterns clearly shows that sulfur doped MBI didn't contain any impure phase from the precursors and bismuth sulfide.

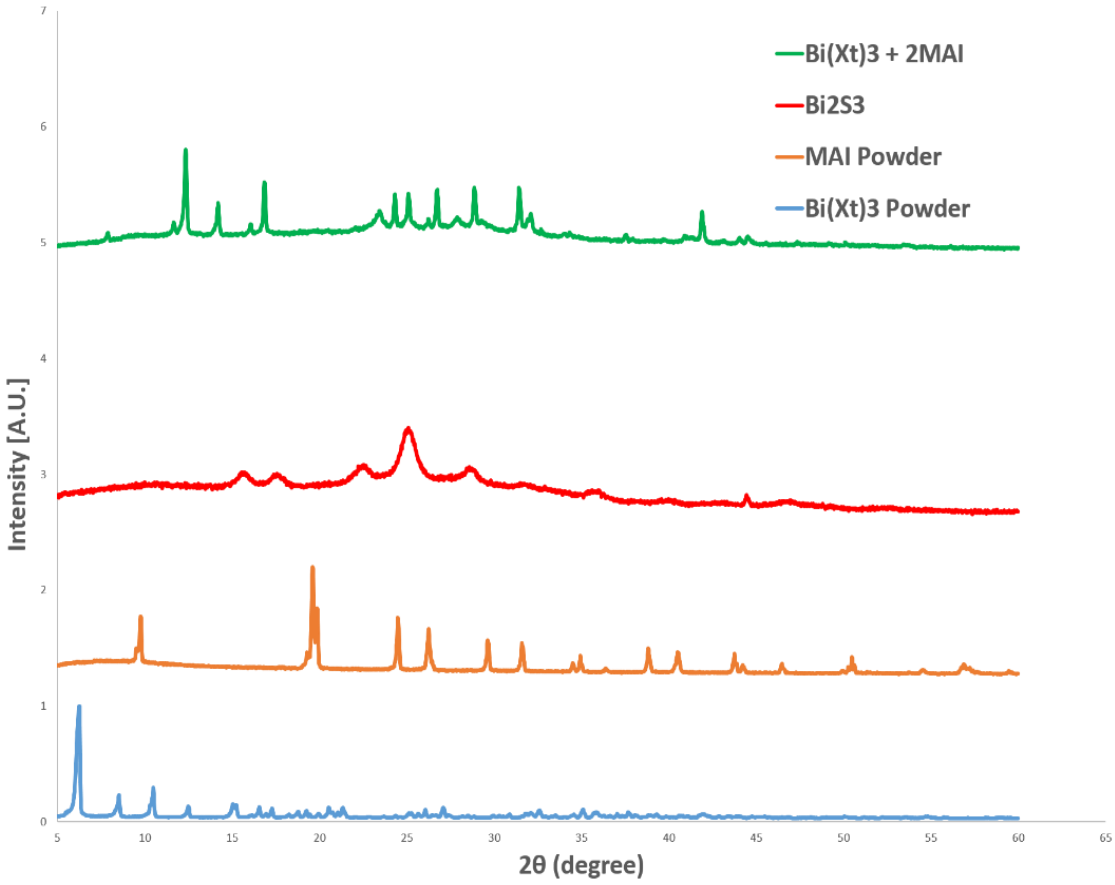

Figure 2. Comparison of sulfur doped MBI XRD Patterns with precursor materials and bismuth sulfide (a) $Bi(xt)_3$ + 2MAI at 150°C (b) Bismuth sulfide powder (c) Methyl ammonium iodide powder (d) Bismuth ethyl xanthate powder.

4.3.3 Bandgap measurement using optical absorption technique

Figure 3 shows the electronic absorption spectra for thin films of the perovskites formed after post annealing of $Bi(xt)_3$ and MAI taken in the molar stoichiometry of 1:2 at different temperatures. Before the measurement of absorption spectra of our samples mesoporous TiO_2 films were used as the reference for excluding the absorption provided by the TiO_2 layer since our sulfur doped MBI was coated above the mesoporous TiO_2 surface. From the Figure 3, it can be clearly seen that thin film obtained after heating at 80°C forms relatively wide bandgap material

and there was a clear red shift in the optical absorption edge as the post heating temperature and was increased above 80°C.

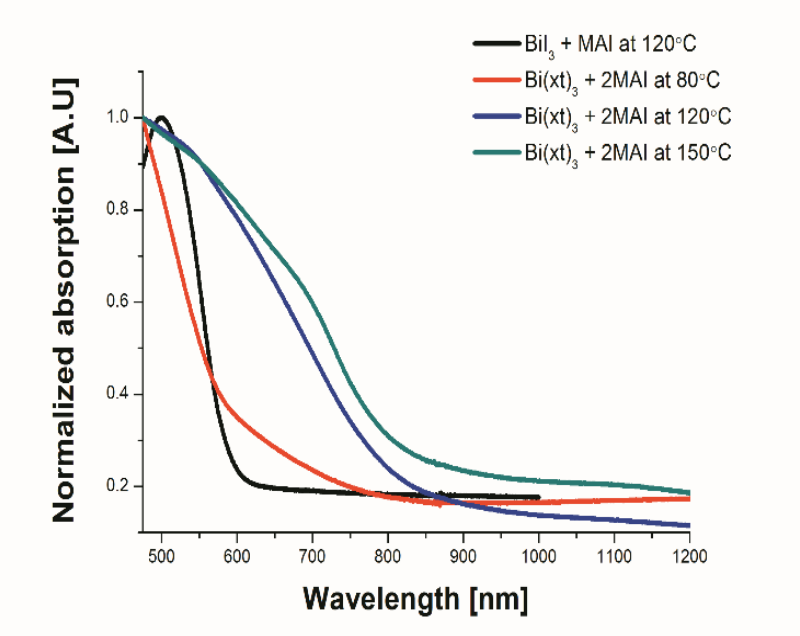

Figure 3. UV-Visible absorption spectra for undoped and sulfur doped MBI at various post heating temperatures.

Absorption spectrum of undoped MBI films having lower optical absorption edge clearly explain the red-shift observed in the present case is attributed to the presence of sulfur moieties in the MBI. In order to estimate the optical bandgap, Tauc plots were made by plotting $(\alpha h\nu)^2$ as a function of photon energy as shown in the Figure 4. A perusal of Tauc plots depicts that the optical bandgap of sulfur doped MBI formed after heating at different temperature leads to lowering of optical bandgap from 2.04 eV (Undoped MBI) to 1.45 eV. In our novel synthesis process bandgap of sulfur doped MBI was decreased as a function of increasing post-heating temperatures. MBI synthesized and reported till date possess optical bandgap of about 2 eV (2.1-2.4 eV) while the bandgap measured in the present case is much lower. This could only be possible considering in-situ sulfur doping of MBI during the decomposition of $Bi(xt)_3$ that drastically reduce the bandgap of the material from 2.04 eV to 1.45 eV which is even lower than the conventional lead halide perovskites.[22] The sample annealed at 80°C was orange in color with blue-shifted absorption

edge resulting in to relatively higher bandgap. This could be probably due to the presence of impurities from the $Bi(xt)_3$ and incomplete doping of sulfur.

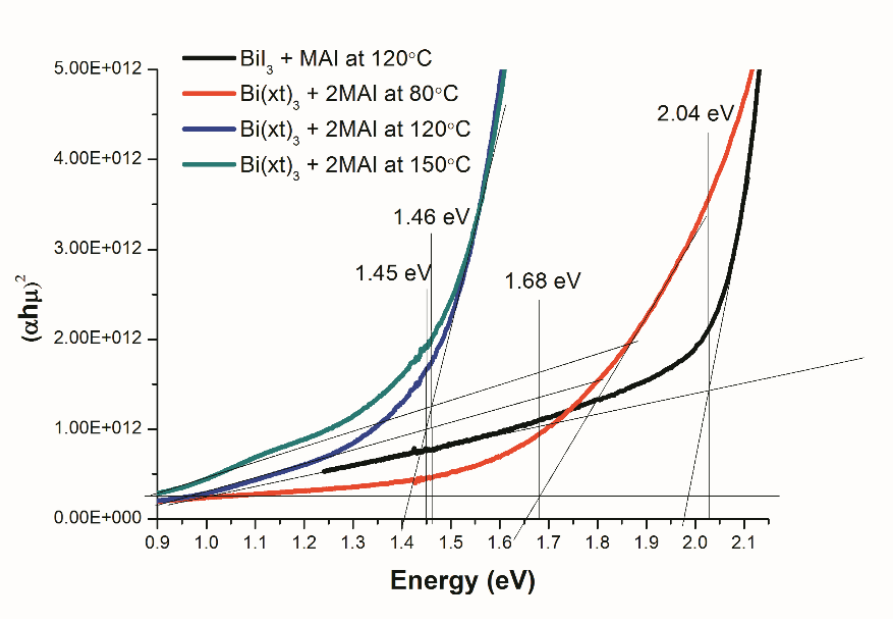

Figure 4. Tauc plots for undoped and sulfur doped MBI at various post heating temperatures.

4.3.4 FTIR measurement

In order to further verify the formation of sulfur doped MBI, FTIR spectroscopic investigations were also conducted and results are shown in the Figure 5. For the measurement of FTIR the powder of the samples were obtained by scratching the sulfur doped MBI on the glass sample. Due to high sensitivity of the FTIR very little powder samples was used for the measurement. The stretching vibrations associated with the C-O-C and C-S bonds of $Bi(xt)_3$ were found at 1210 cm^{-1} and 1025 cm^{-1} respectively. Even after annealing the sulfur doped MBI at 80°C intense bands for C-O-C and C-S linkages were still seen, suggesting that $Bi(xt)_3$ was not decomposed completely. In addition, C-N stretching vibration was also found at 1113 cm^{-1} for the samples post heated at 80°C which should be originated from the solvent DMF.[23] Interestingly, the C-O-C and C-S bond vibrations of $Bi(xt)_3$ and DMF were completely vanished for the samples annealed at temperature >120°C. The typical vibration bands for MBI like N-H stretching at 3178

cm^{-1}, N-H bending at 1581 cm^{-1}, N-H wagging at 909 cm^{-1}, and C-H bending vibration at 1468 cm^{-1} can be clearly seen. The samples annealed at 150°C also had the similar groups with minor shift in the peak position.

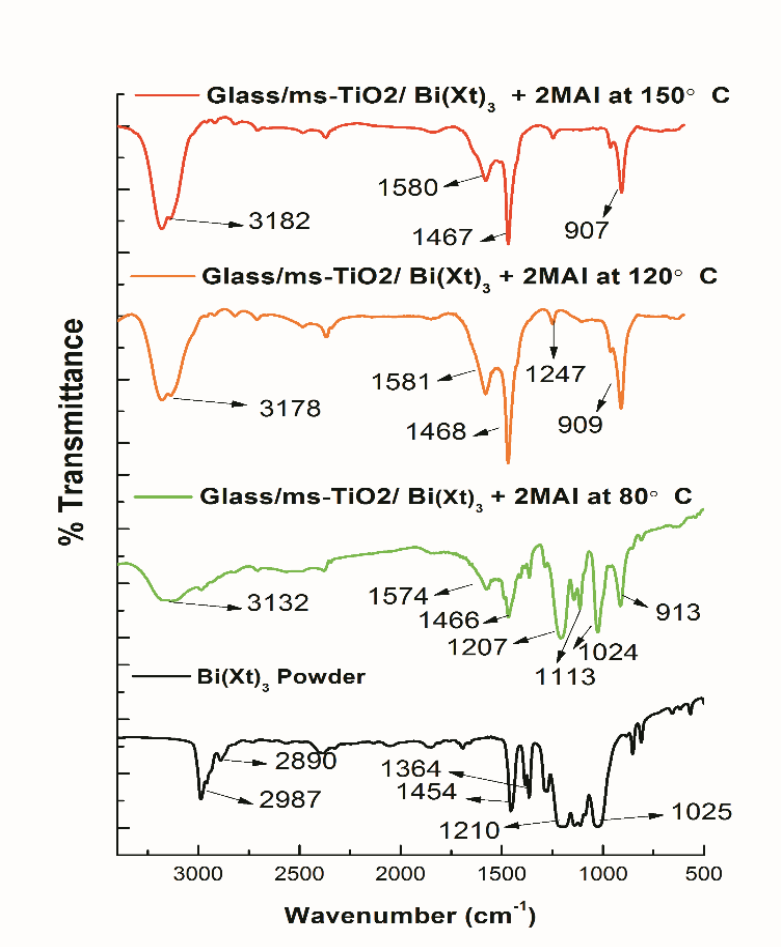

Figure 5. FTIR spectrum of $Bi(xt)_3$ powder and sulfur doped MBI at different temperatures.

4.3.5 Optimization of post annealing temperature using TGA

For optimizing the post annealing temperature and to know the decomposition temperature of $Bi(xt)_3$, TG-DTA measurement was performed as shown in the Figure 6. It can be seen that $Bi(xt)_3$ starts decomposing at 120°C. The expected and observed residual weight percentage from 120°C -160°C showed the formation of Bi_2S_3. Therefore, it is the clear evident that for making sulfur doped MBI minimum post heating of 120°C is required to remove the organic impurities from $Bi(xt)_3$ and for complete doping of sulfur. Thus results obtained from investigations

pertaining to the FTIR and TG-DTA reveal the reason for change in color from orange to black and reduction in the bandgap from 1.68 eV to 1.45 eV when sulfur doped MBI was post annealed at 120^{o}C-150^{o}C.

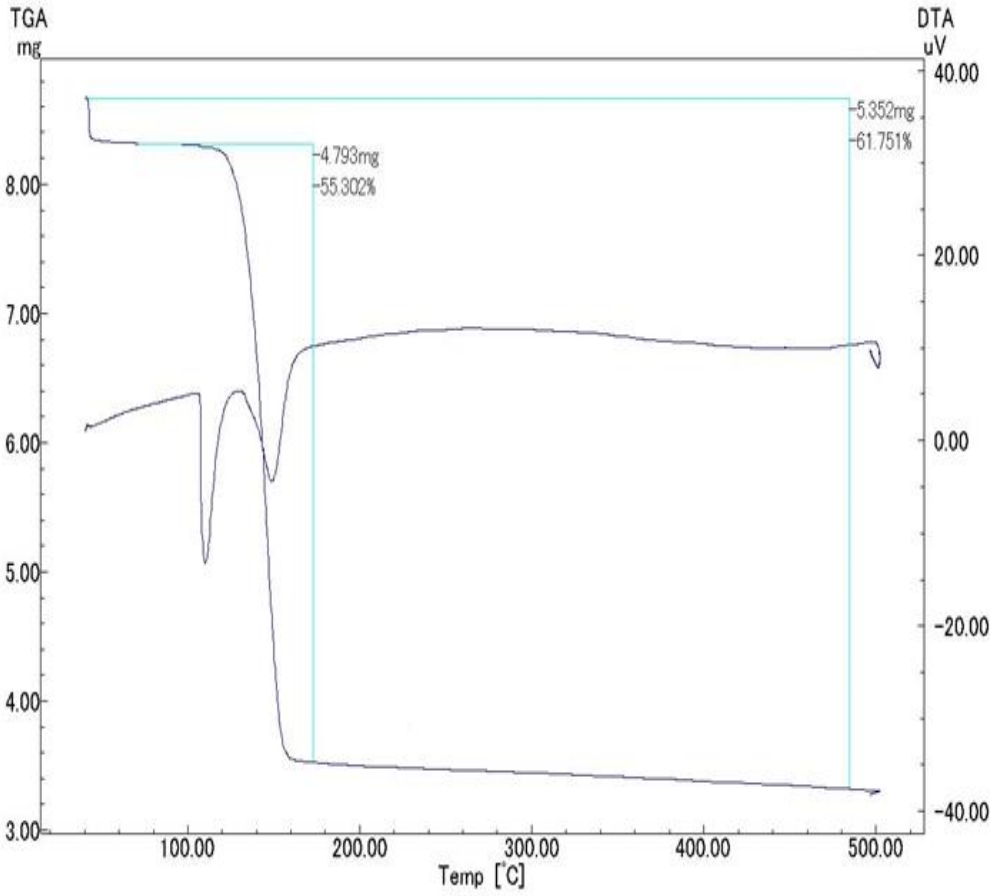

Figure 6. TG-DTA for Bi(xt)$_3$ powder.

4.3.6 Elemental composition studies by X-ray photoelectron spectroscopy (XPS)

Elemental composition of the sulfur doped MBI was further probed by XPS measurement and wide energy survey spectrum was shown in the Figure 7. A perusal of XPS survey spectrum reveals the presence of Bi, I, S, C, N, Ti and O atoms. Origin of Ti and O which are basically from the mesoporous TiO_2 layer. In bismuth presence of Bi 4p, Bi 4d, Bi 5d, and Bi 4f was observed, while in the case of sulfur S 2p was noted. In case of iodine I 3d and I 4d was present.

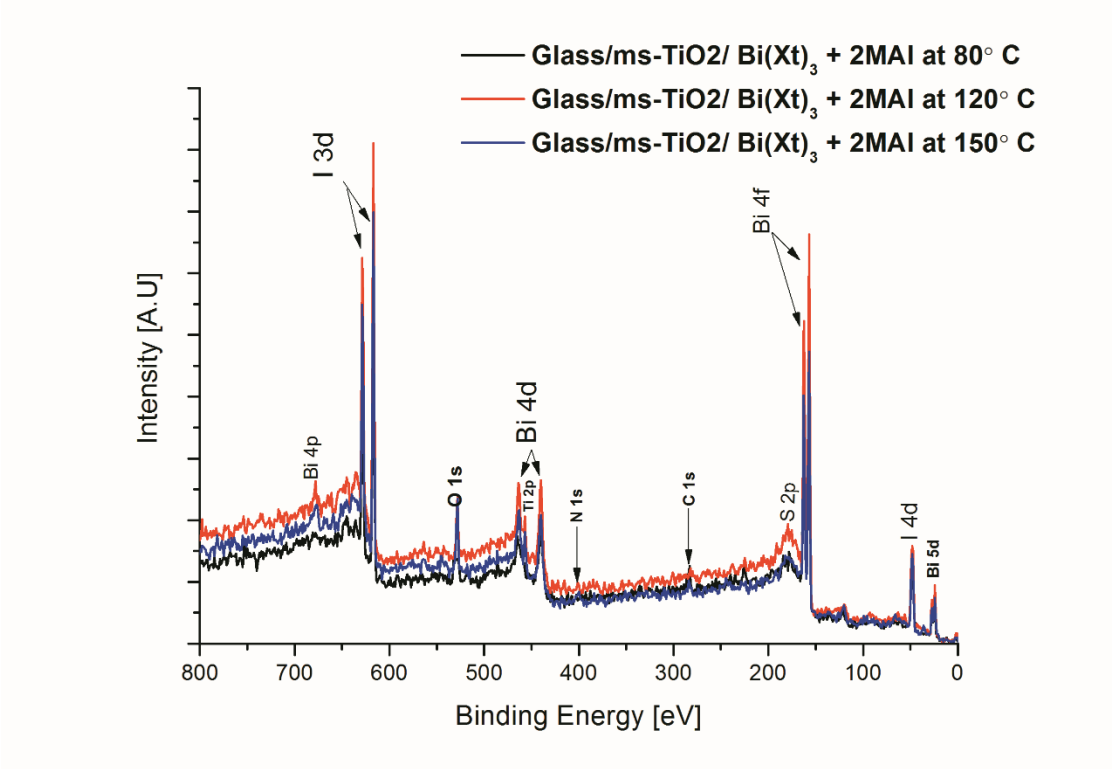

Figure 7. XPS spectra of sulfur doped MBI at different temperatures in wide range.

The main aim for doing the XPS studies was primarily to prove the presence of sulfur in the system because in the case of chloride additives no traces of Cl^- ions were found but changes the property of the perovskite material. So, presence of peak related to S 2p clearly indicates the presence of sulfur in the system. High resolution XPS analysis for Bi(4f) and S(2p) orbitals are shown in the Figure 8. The binding energy of Bi $4f_{7/2}$ was 158.8 eV for the samples post heated at 80°C and 120°C while samples post heated at 150°C exhibited the binding energy slightly shifted at 158.6 eV. Observed values of the binding energy are in very good agreement with the reported values of MBI [6] clearly indicating that sulfur present in the system didn't change the chemical bonding environment of Bi. Interestingly, S $2p_{3/2}$ peaks had the notable peak shift from 162.3 eV (sample post heated at 80°C) to 161.3 eV (sample post heated at 150°C). This reduction in binding energy shows that addition of valence electron charge which is most probably due to the complete removal of organic impurities from the xanthates.

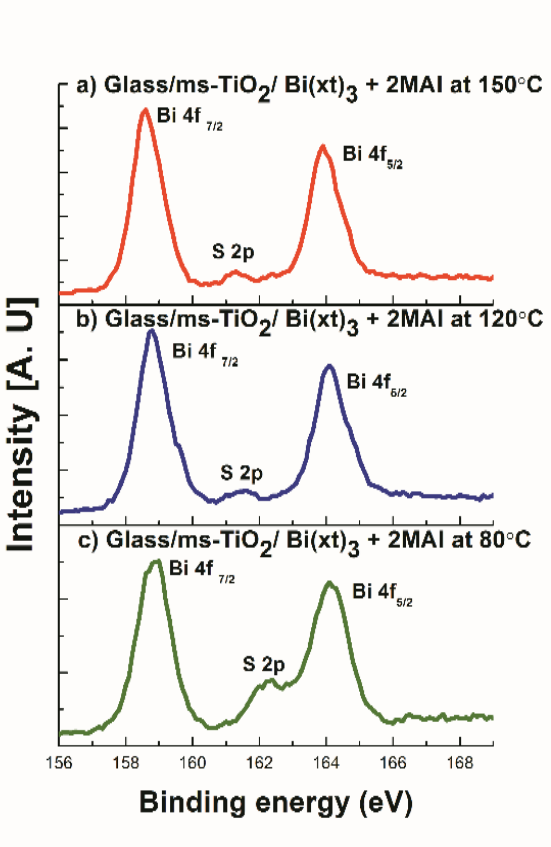

Figure 8. High resolution XPS spectra for Bi 4f and S 2p of sulfur doped MBI at various post heating temperatures.

4.3.7 HOMO measurement using photoelectron yield spectroscopy (PYS)

Sulfur doped MBI was also subjected to photoelectron yield spectroscopic (PYS) measurements and results are shown in the Figure 9. HOMO energy level for the samples post heated at 80°C was found to be -5.08 eV while further increase in temperature led to decrease in the HOMO level to - 5.65 eV for the samples annealed at 120°C-150°C. In combination with band gap estimated from Tauc plot and HOMO by PYS, LUMO energy levels for sulfur doped MBI were also calculated to construct the energy band diagram as shown in Figure 10. From the energy band diagram, it is clear that sulfur doped MBI annealed at 120°C and 150°C can work well with

commonly used HTM like spiro-OMeTAD or P3HT while ETL with relatively deeper LUMO like SnO_2 would be suitable for the photovoltaic applications. [24]

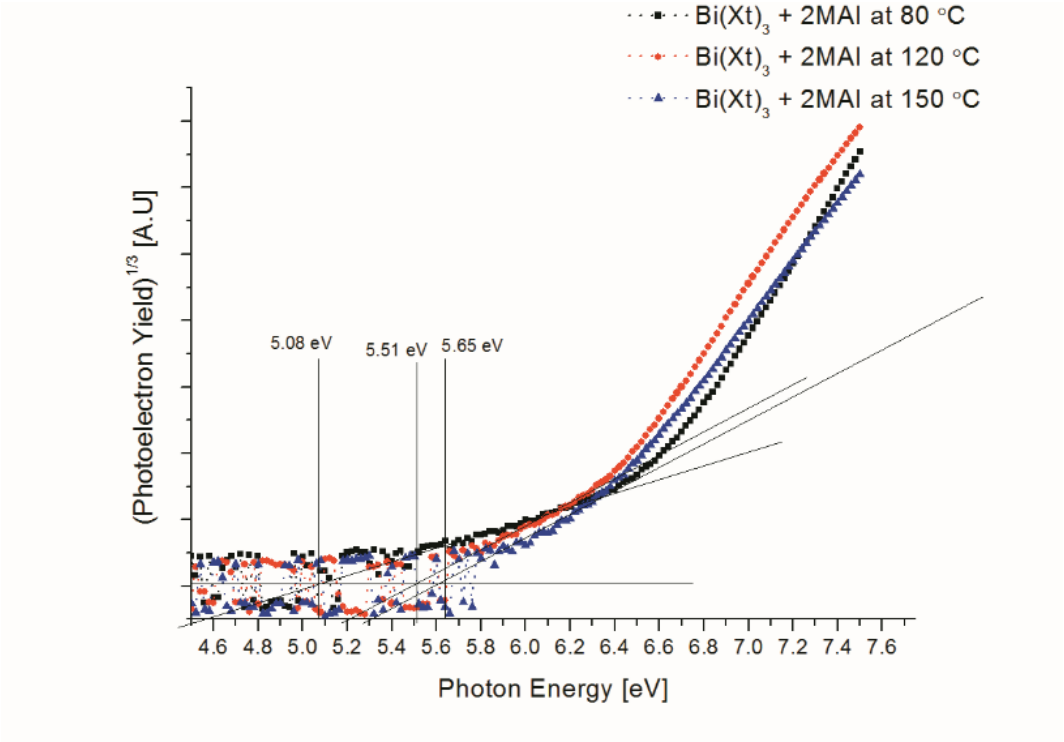

Figure 9. Photoelectron yield spectroscopy of sulfur doped MBI post annealed at different temperature.

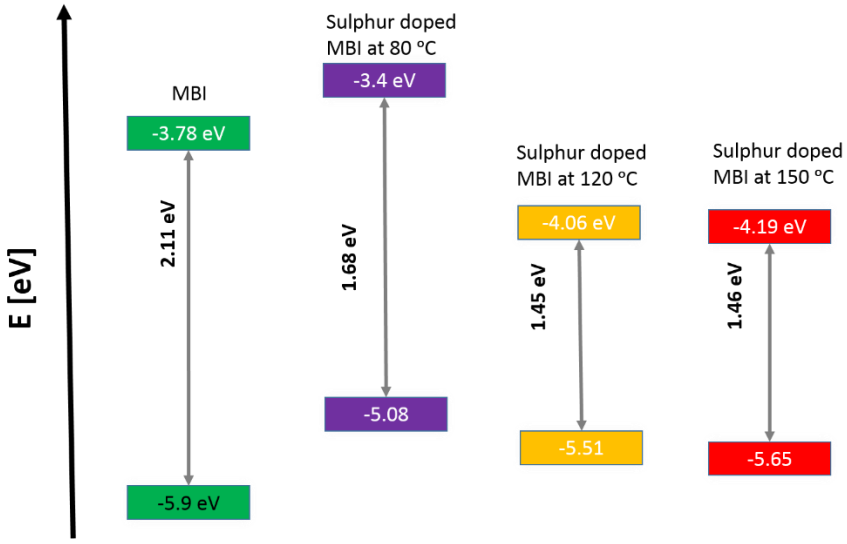

Figure 10. Energy band diagram for undoped MBI and sulfur doped MBI post heated at different temperatures

4.3.8 Investigation of electronic studies by Hall-effect measurement

Hall-Effect measurement was also conducted in order to investigate their electronic characteristics like nature, conductivity, carrier concentration, and carrier mobility. All of the sulfur doped MBI films exhibited the P-type semiconducting behavior due to the observation of positive Hall coefficients. Samples post heated at 120^{o}C exhibited carrier concentration of 2.3 × 1021 cm^{-3} along with the high carrier mobility of 2.28 $cm^2.v^{-1}s^{-1}$. This obtained carrier concentration for our sample is more than 7 orders of magnitude higher than conventional $MAPbI_3$ and 5 orders of magnitude higher than undoped MBI as shown in Table 1.

Table 1. Comparison of Hall-Effect measurement

Material	Carrier concentration	Mobility
Sulfur doped MBI at 120^{o}C	2.3×10^{21} cm^{-3}	2.28 $cm^2.v^{-1}s^{-1}$
Undoped MBI	10^{16} cm^{-3}[1]	1 $cm^2.v^{-1}s^{-1}$ [1]
Lead perovskites ($MAPbI_3$)	2.7×10^{14} cm^{-3} [2]	8.2 $cm^2.v^{-1}s^{-1}$ [3]

4.3.9 Photoluminescence spectroscopy (PL measurement)

Figure 11 shows the PL measurement for sulfur doped MBI samples post annealed at different temperatures. The time taken by the electron to decay from the PL can be taken as the PL decay time. By PL measurement at room temperature we cannot distinctly say whether the PL decay corresponds to exciton or free charge carrier lifetime unless knowing the exciton binding energy. However, the recombination time of the photo-excited species could be measured. Life time measured for the sulfur doped MBI was given in the Table 2 and also detailed comparison with undoped MBI and lead based perovskites are also given. The life time of the samples seems to be increasing in relation with post annealing temperature. The maximum life time of 0.91 ns was obtained for the samples post annealed at 150°C. The life time obtained for the sulfur doped MBI was almost 8 times higher than that of conventional undoped MBI. However it is comparatively low than lead based perovskites $MAPbI_3$.

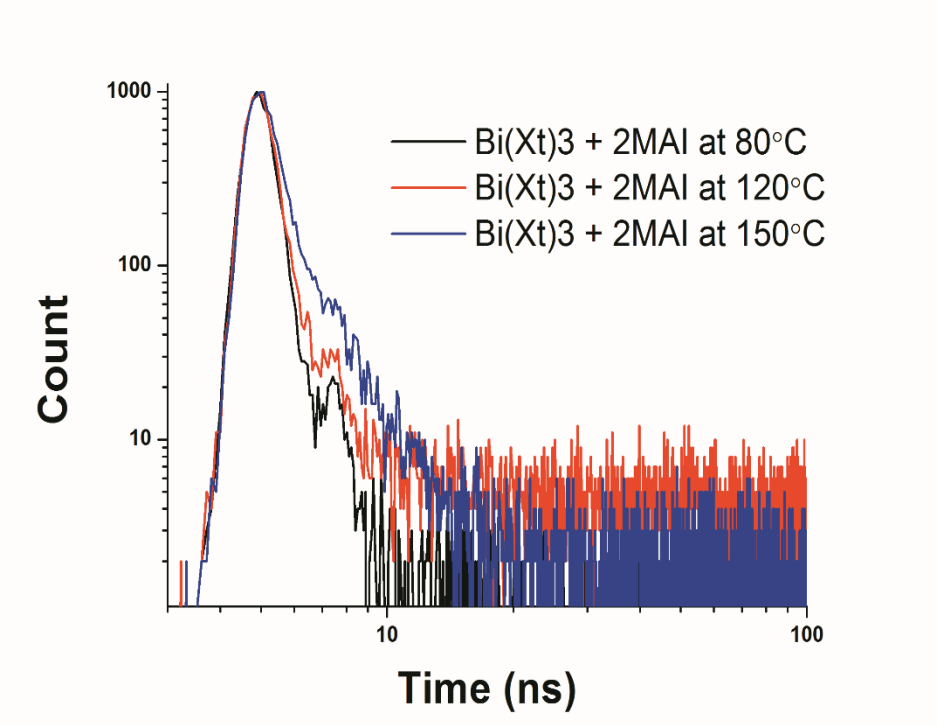

Figure 11. Photoluminescence spectroscopy of sulfur doped MBI post annealed at different temperature.

Table 2. Life time measurement of sulfur doped MBI and its comparison

Sample details	Life time
$Bi(xt)_3$ + 2MAI annealed at 80°C	0.63 ns
$Bi(xt)_3$ + 2MAI annealed at 120°C	0.85 ns
$Bi(xt)_3$ + 2MAI annealed at 150°C	0.91 ns
Undoped MBI	0.12 ns
Lead based perovskites ($MAPbI_3$)	2 ns

4.3.10 Surface morphology studies (FE-SEM)

FE-SEM analysis was made for examining the surface morphology of sulfur doped MBI samples and has been shown in the Figure 12. For this purpose, material was spin coated on the glass slide without mesoporous TiO_2 layer. Samples heated at 80^{o}C exhibited featureless amorphous surface without clearly visible isolated particles which could be attributed to the presence of remaining solvent (DMF) as indicated from FTIR. Interestingly, samples post heated at 120^{o}C exhibited needle shaped particles with relatively better surface coverage.

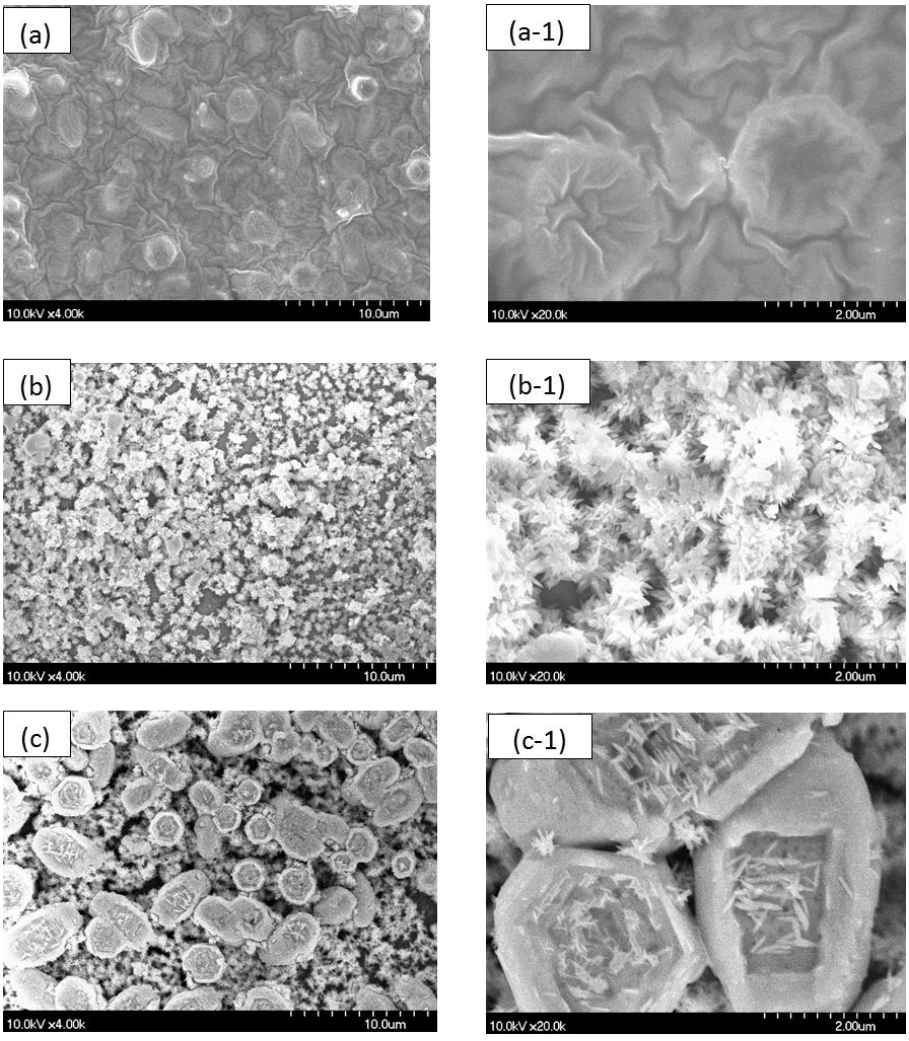

Figure 12. FE-SEM images of sulfur doped MBI post annealed at different temperature (a and a-1) 80^{o}C, (b and b-1) 120^{o}C, (c and c-1) 150^{o}C.

4.4 Conclusions

In summary, existing problem of bandgap reduction in MBI for extended wavelength photon harvesting was amicably solved by demonstration of facile and convenient preparation of sulfur doped MBI. This sulfur doped MBI was prepared by in-situ doping of sulfur via thermal decomposition of $Bi(xt)_3$ leading to the formation novel perovskite having band gap even lower than that of most widely used $MAPbI_3$. XRD results showed the similar profile related to undoped MBI suggesting the presence of sulfur in the interstitial sites. The presence of sulfur also was confirmed by the XPS measurement. Minimum temperature for making sulfur doped MBI was found to be 120^{o}C as indicated by FTIR and TG-DTA investigations. Hall-Effect studies suggested that obtained samples are P-type semiconductor with higher carrier concentration and mobility as compared to that of undoped MBI. From the PL measurement 0.91 ns life time was obtained for sulfur doped MBI which is higher than the conventional undoped MBI. Results of the present work indicate that such materials could be one of prospective candidates towards the development of lead free and stable perovskite solar cells in future.

4.5 References

(1) http://www.nrel.gov/ncpv/images/efficiency_chart.jpg

(2) Yu, Z.; Sun, L. Recent Progress on Hole-Transporting Materials for Emerging Organometal Halide Perovskite Solar Cells. *Adv. Energy Mater*. 2015, 5, 1500213.

(3) Völker, S. F.; Collavini, S.; Delgado, J. L. Organic Charge Carriers for Perovskite Solar Cells. *ChemSusChem*. 2015, 8, 3012–3028.

(4) Hao, F.; Stoumpos, C. C.; Cao, D. H.; Chang, R. P. H.; Kanatzidis, M. G. Lead-Free Solid-State Organic–inorganicHalide Perovskite Solar Cells. *Nat. Photonics* 2014, 8, 489–494.

(5) Noel, N. K.; Stranks, S. D.; Abate, A.; Wehrenfennig, C.; Guarnera, S.; Haghighirad, A.-A.; Sadhanala, A.; Eperon, G. E.; Pathak, S. K.; Johnston, M. B.; Petrozza, A.; Herz, L. M.; Snaith, H. J. Lead-Free Organic-Inorganic Tin Halide Perovskites for Photovoltaic Applications. *Energy Environ. Sci.* 2014, *7*, 3061–3068.

(6) Lyu, M.; Yun, J.-H.; Cai, M.; Jiao, Y.; Bernhardt, P. V; Zhang, M.; Wang, Q.; Du, A.; Wang, H.; Liu, G.; Wang, L. Organic-Inorganic Bismuth (III)-Based Material: A Lead-Free, Air-Stable and Solution-Processable Light-Absorber beyond Organolead Perovskites. *Nano Res.* 2016, *9*, 692–702.

(7) Kawai, T.; Shimanuki, S. Optical Studies of $(CH_3NH_3)_3Bi_2I_9$ Single Crystals. *Phys. status solidi* 1993, *177*, K43–K45.

(8) Park, B.-W.; Philippe, B.; Zhang, X.; Rensmo, H.; Boschloo, G.; Johansson, E. M. J. Bismuth Based Hybrid Perovskites $A_3Bi_2I_9$ (A: Methylammonium or Cesium) for Solar Cell Application. *Adv. Mater.* 2015, *27*, 6806–6813.

(9) Oz, S.; Hebig, J. C.; Jung, E.; Singh, T.; Lepcha, A.; Olthof, S.; Jan, F.; Gao, Y.; German, R.; van Loosdrecht, P. H. M.; Meerholz, K.; Kirchartz, T.; Mathur, S. Zero-Dimensional $(CH_3NH_3)_3Bi_2I_9$ Perovskite for Optoelectronic Applications. *Sol. Energy Mater. Sol. Cells*. doi: 10.1016/j.solmat.2016.01.035.

(10) Saparov, B.; Hong, F.; Sun, J.-P.; Duan, H.-S.; Meng, W.; Cameron, S.; Hill, I. G.; Yan, Y.; Mitzi, D. B. Thin-Film Preparation and Characterization of $Cs_3Sb_2I_9$: A Lead-Free Layered Perovskite Semiconductor. *Chem. Mater.* 2015, 27, 5622–5632.

(11) Mitzi, D. B. Templating and Structural Engineering in Organic-Inorganic Perovskites. *J. Chem. Soc. Dalt. Trans.* 2001, 1–12.

(12) Mitzi, D. B.; Wang, S.; Feild, C. A.; Chess, C. A.; Guloy, A. M. Conducting Layered Organic-Inorganic Halides Containing -Oriented Perovskite Sheets. Science. 1995, 267, 1473–1476.

(13) Sun, S.; Tominaka, S.; Lee, J.-H.; Xie, F.; Bristowe, P. D.; Cheetham, A. K. Synthesis, Crystal Structure, and Properties of a Perovskite-Related Bismuth Phase, $(NH_4)_3Bi_2I_9$. *APL Mater.* 2016, 4, 031101.

(14) Slavney, A. H.; Hu, T.; Lindenberg, A. M.; Karunadasa, H. I. A Bismuth-Halide Double Perovskite with Long Carrier Recombination Lifetime for Photovoltaic Applications. *J. Am. Chem. Soc.* 2016, 138, 2138–2141.

(15) Sun, Y.; Shi, J.; Lian, J.; Gao, W.; Agiorgousis, M. L.; Zhang, P.; Zhang, S. Discovering Lead-Free Perovskite Solar Materials with Split-Anion Approach. *Nanoscale* 2016, 8, 6284-6289.

(16) Vreugdenhil, A. J.; Brienne, S. H. R.; Butler, I. S.; Finch, J. a.; Markwell, R. D. Infrared Spectroscopic Determination of the Gas-Phase Thermal Decomposition Products of Metal-Ethyldithiocarbonate Complexes. Spectrochim. *Acta Part A Mol. Biomol. Spectrosc.* 1997, 53, 2139–2151.

(17) Bryndzia, L. T.; Kleppa, O. J. Standard Enthalpies of Formation of Sulfides and Sulfosalts in the Ag-Bi-S System by High-Temperature, Direct Synthesis Calorimetry. *Econ. Geol.* 1988, 83, 174–181.

(18) Cubicciotti, D. Enthalpy of Formation of bismuth(III) Iodide and the Dissociation Energy of bismuth(I) Iodide. *Inorg. Chem.* 1968, 7, 211–213.

(19) Hoye, R. L. Z.; Brandt, R. E.; Osherov, A.; Stevanovic, V.; Stranks, S. D.; Wilson, M. W. B.; Kim, H.; Akey, A. J.; Perkins, J. D.; Kurchin, R. C.; Poindexter, J. R.; Wang, E. N.; Bawendi, M. G.; Bulovic, V.; Buonassisi, T. Methylammonium Bismuth Iodide as a Lead-Free, Stable Hybrid Organic-Inorganic Solar Absorber. *Chem. - A Eur. J.* 2016, 22, 2605–2610.

(20) Eckhardt, K.; Bon, V.; Getzschmann, J.; Grothe, J.; Wisser, F. M.; Kaskel, S. Crystallographic Insights into $(CH_3NH_3)_3(Bi2I_9)$: A New Lead-Free Hybrid Organic-Inorganic Material as a Potential Absorber for Photovoltaics. *Chem. Commun.* 2016, 52, 3058–3060.

(21) Cui, D.; Yang, Z.; Yang, D.; Ren, X.; Liu, Y.; Wei, Q.; Fan, H.; Zeng, J.; Liu, S. (Frank). Color-Tuned Perovskite Films Prepared for Efficient Solar Cell Applications. *J. Phys. Chem. C* 2015, 120, 42–47.

(22) Murugan, V.; Ogomi, Y.; Pandey, S. S.; Toyoda, T.; Shen, Q.; Hayase, S. Effects of Different Chloride Precursors on Crystal Growth of Lead Halide Perovskites. *Appl. Phys. Express* 2015, 8, 125501.

(23) Guo, X.; McCleese, C.; Kolodziej, C.; Samia, A. C. S.; Zhao, Y.; Burda, C. Identification and Characterization of the Intermediate Phase in Hybrid Organic-Inorganic $MAPbI_3$ Perovskite. *Dalton Trans.* 2016, 45, 3806-3813.

(24) Salim, T.; Sun, S.; Abe, Y.; Krishna, A.; Grimsdale, A. C.; Lam, Y. M. Perovskite-Based Solar Cells: Impact of Morphology and Device Architecture on Device Performance. *J. Mater. Chem. A*. 2015, 3, 8943–8969.

Chapter 5. General Conclusion

Crystal growth, morphology and surface coverage are the important parameters to achieve high efficiency in lead based perovskites. There are various kinds of methods to solve these issues in the lead based perovskites like by increasing the precursor ratio, solvent engineering, vacuum assisted PVD techniques etc. But we chose to add chloride as additives to overcome the problem. We achieved the grain size almost double when compared to the samples without additives. Also study on the impact of different chloride precursors was studied. As another part of my doctorate studies we also found the novel lead free bismuth based perovskites with narrow bandgap. In the conventional bismuth based perovskite wider bandgap is the huge bottleneck, we solved this problem by doping sulfur in to the bismuth based perovskites. The bandgap we achieved was lower even when compared to the lead based perovskites which was the very big achievement. To best of our knowledge our work done is the first element of investigation on both lead based and lead free perovskites.

In the first chapter of the thesis basic importance and types of renewable energy were discussed. In that specific role of solar energy was discussed in detail. Various kinds of materials involved in solar energy application was also discussed in brief. In that importance perovskite materials as light absorbers was given in accordance with their unique physical and chemical properties. A brief introduction on perovskite structure and relative change in properties were highlighted. The basic aim and idea about the current thesis were explained in detail subsequently.

Second chapter gives the fundamentals and basic ideas for the instrumentations that was utilized. Mainly all the instruments were used for studying the variation in the physical properties of lead based and lead free perovskites. A brief details about the working principles of each instruments was also discussed with literature proofs to understand its mechanism.

Chapter three was focused on the investigation of lead based perovskites with introduction about the experimental parameters followed to make lead based perovskite films. By using different kinds of chloride precursors, Ethyl ammonium chloride (EACl) was found as the best additive for the bigger grain size growth of lead based perovskites. XRD was employed to mainly study the crystal nature of the perovskites and it was found that grain size was almost double when compared to the other samples. The impact of alkyl chain length in different chloride precursors

over the crystal growth studied through their XRD pattern. It has been shown that dissociation of Cl^- ions plays the crucial role in fixing the crystal size of the perovskites. From the FE-SEM it was proved that grain size growth was bigger than lead based perovskites without additives with better surface coverage. In addition different anion like Br, and I was also substituted in the EACl to study the role of anion crystal growth. Photoacoustic characterization was done to know bandgap variations, reduce in the defect of the crystal by urbach energy and secondary proof to increase in grain size (Steepness factor). The bandgap didn't had any variation due to the additives and defects highly reduced due to EACl as additive. All the results obtained from the photoacoustic studies was completely supportive to other characterization techniques utilized. Finally to improve the lead based perovskite surface smooth, EACl was used in two-step crystal growth of lead based perovskites. In this context, different solvents like DMF and DMSO were used for growing the smooth surface. Again through XRD studies clear increase in grain size was found and in addition AFM technique was used to study the roughness and showed the smooth surface for the samples used DMSO solvent. From all the above experiment it was concluded that EACl as the best additive with DMSO as the solvent in the two step methodology.

Fourth chapter deals with the lead free bismuth based perovskites. A novel approach to make bismuth based perovskites films using bismuth xanthate was explained in the experimental part with appropriate characterization techniques. The confirmation of the material phase was studied through XRD with the simulated pattern of undoped bismuth perovskites. From UV-Visible spectroscopy clear shift in band edge was observed from 2.04 eV (Undoped) to 1.45 eV (Sulfur doped) which is the very big breakthrough in the field of lead free perovskites. The presence of sulfur also was confirmed by the XPS measurement. FTIR and TG-DTA investigations showed that minimum temperature for making sulfur doped MBI was 120^{o}C. Hall-Effect studies suggested that obtained samples are P-type semiconductor with higher carrier concentration and mobility as compared to that of undoped MBI. From the PL measurement 0.91 ns life time was obtained for sulfur doped MBI which is higher than the conventional undoped MBI. All these parameters shows that sulfur doped MBI will be one of the best competitor in the field of solar cells.

Future prospect

In the future prospect the lead based perovskites with EACl ($CH_3NH_3PbI_{3-x}Cl_x$) as additive could be employed in the planar architecture (p-i-n). Because in planar architecture the perovskite material with high diffusion length is required in order to achieve the high efficiency. In $CH_3NH_3PbI_{3-x}Cl_x$ kind of perovskites already proved that it has the high diffusion length when compared to that of $CH_3NH_3PbI_3$. So, best part of our work is in addition to these property we also demonstrated the way to grow bigger and less defect $CH_3NH_3PbI_{3-x}Cl_x$ crystals using EACl. All these studies clearly shows that lead based perovskites with EACl as additive will be one of the potential candidate in the field of planar architecture (p-i-n) solar cells. This material can also act the important candidate in flexible perovskite solar cells where p-i-n or n-i-p structures are used. By careful evaluation and strategy EACl additive has much chances for enhancing the performances of lead based perovskites in planar architecture rather than meso-structured devices. Further investigation of EACl additive with other types of perovskite like $CsPbI_3$, $FAPbI_3$, and $MA_3Bi_2I_9$ could reveal lot more interesting physicochemical properties that may be useful in enhancing the solar cell performance.

For sulfur doped MBI careful we have fabricated our device in the configuration of FTO/Compact TiO_2/ Mesoporous TiO_2/ Sulfur doped MBI/Spiro-OMeTAD/Gold. Very good ideal diode characteristics was observed for Sulfur doped MBI. However, more focus is required in order to obtain the high efficiency since it is controlled by a lot of optimization issues of various other components and interfaces. In that part, from our opinion the reason for poor performance could be the electron transport layer. The HOMO of our material is 4.06 ~ 4.19 eV which is lower than that of mesoporous TiO_2 with HOMO of 4 eV. This issue is also applicable to the compact layer TiO_2 which apparently shows that conventional device architecture for $MAPbI_3$ (Methyl ammonium lead iodide) perovskites could not be applicable to sulfur doped MBI. So, lot of efforts is needed in choosing the suitable materials for electron transport and compact layer for achieving high photovoltaic performance. This novel finding of sulfur doped $MA_3Bi_2I_9$ to reduce the bandgap by $Bi(xt)_3$ (xt = Ethyl Xanthate) may not only the breakthrough in improving the performance of $MA_3Bi_2I_9$, but also usage of Sn, Sb or Pb xanthate with MAI has higher possibility to deliver novel materials in future.

Achievements

(A) Publications:

- Murugan Vigneshwaran*; Ohta, T.; Iikubo, S.; Kapil, G.; Ripolles, T. S.; Ogomi, Y.; Ma, T.; Pandey, S. S.; Shen, Q.; Toyoda, T.;Yoshino,K.; Minemoto, T.; Shuzi Hayase. "**Facile Synthesis and Characterization of Sulfur Doped Low Bandgap Bismuth Based Perovskites by Soluble Precursor Route**". **ACS Chemistry of Materials**, 2016. DOI: acs.chemmater.6b02315. (Impact factor: 9.4)

- Murugan Vigneshwaran*, Ogomi, Y., Pandey, S. S., Toyoda, T., Shen, Q., & Shuzi Hayase (2015). "**Effects of different chloride precursors on crystal growth of lead halide perovskites**". **Applied Physics Express**, 8(12), 125501. (Impact Factor: 2.3)

(B) National and International conferences

1. "Facile Synthesis and Characterization of Sulfur Doped Low Bandgap Bismuth Based Perovskites by Soluble Precursor Route**"** Murugan Vigneshwaran, Takeshi Ohta, Satoshi Iikubo, Gaurav Kapil, Teresa Ripolles, Yuhei Ogomi, Tingli Ma, Shyam S. Pandey, Qing Shen, Taro Toyoda, Kenji Yoshino, Takashi Minemoto, Shuzi Hayase: **HOPV, Yokahama, Japan, 2-4 February, 2017**. (Poster)
2. **"**Investigation of lead free novel perovskites prepared by facile route for solar cell applications" Murugan Vigneshwaran, Takeshi Ohta, Satoshi Iikubo, Gaurav Kapil, Teresa Ripolles, Yuhei Ogomi, Tingli Ma, Shyam S. Pandey, Qing Shen, Taro Toyoda, Kenji Yoshino, Takashi Minemoto, Shuzi Hayase: **77th autumn meeting of Japan Applied Physics Society**, Toki Messe, Niigata, Japan 13-16 September, 2016. (ORAL)
3. **"**Sulfur doped lower band gap bismuth based perovskites for future solar cells**"** Murugan Vigneshwaran, Takeshi Ohta, Satoshi Iikubo, Gaurav Kapil, Teresa Ripolles, Yuhei Ogomi, Tingli Ma, Shyam S. Pandey, Qing Shen, Taro Toyoda, Kenji Yoshino, Takashi Minemoto, Shuzi Hayase: **MRS-Japan, 18-20 December, 2016**. (ORAL)
4. "Selection of Suitable Chloride Precursor for Bigger Crystal Growth and Reduced Defects in Lead Halide Perovskites" Murugan Vigneshwaran, Yuhei Ogomi, Shyam S. Pandey, Taro Toyoda, Qing Shen, Shuzi Hayase: International Union of Materials Research

Societies- **International Conference on Electronic Materials (IUMRS-ICEM), Suntec Singapore**, 04-08 July, 2016. (ORAL)

5. "Controlled Crystal Growth of $MAPbI_3$ with Smooth Surface Using EACl and DMSO" Murugan Vigneshwaran, T. Nishimura, Y. Ogomi, S.S Pandey, T. Toyoda, Q. Shen and S. Hayase: **2015-Autumn Meeting of Electrochemical Society, Japan**, Saitama University, September, 2015. (ORAL)

6. "Controlled crystal growth of lead halide perovskites by adding different types of chloride precursors" Murugan Vigneshwaran, T. Nishimura, Y. Ogomi, T. Ma, S.S. Pandey, S. Hayase**: 95th Spring meeting of Japan Chemical Society**, Funabashi Campus, Nihon University, Chiba, Japan, 26-29 March, 2015. (ORAL)

7. "Optimization of suitable chloride precursor for better crystal growth of $MAPbI_3$" Murugan Vigneshwaran, T. Nishimura, Y. Ogomi, T. Ma, S.S. Pandey, S. Hayase**: 62nd spring meeting of Japan Applied Physics Society**, Shonan Campus, Tokai University, Japan March 11-14, 2015. (ORAL)

Acknowledgement

First of all, I would like to thank **Prof. Shuzi Hayase** for giving me opportunity to work under him as PhD scholar. His immense depth of knowledge and insight into the work have pave the excellent background in this work. His charming personality always motivate to tackle the challenges very easily.

I would like to thank **Prof. Shyam Pandey** for his valuable suggestions and fruitful discussion. His enthusiasm and faith in me have created a true passion for work in this field and inspired me to see through all the setbacks I experienced along the way. I would like to add on that his kind and supportive nature has make my stay in Japan very lively. My sincere thanks to **Prof. Takashima**, **Prof. Ma**, and **Ass. Prof Ogomi** for their support in experiments carried out.

I also like to thank my collaborators **Prof. Qing Shen** and **Prof. Taro Toyoda** (The University of Electro-communications), **Prof. Kenji Yoshino** (Miyazaki University), and **Prof. Takashi Minemoto** (Ritsumeikan University).

I acknowledge **Dr. Temuri Nishimura, Mr. Takuya Morimoto, Mr. Moriya Sohei, Mr. Hamada, Mr. Sakamoto, Mr. Shimazaki, and Dr. Takeshi Ohta** for their helping nature and making the lab atmosphere very healthy and charming.

I would also like to thank my lab colleague **Dr. Gaurav Kapil, Dr. Ajaykumar baranwal and Dr. Tarunchand vagavala** for their nice company during my PhD work.

I express my sincere thanks to **Mr. Nayanjyoti baishya, Mr. Mallikarjun yelameli, and Mr. Ravinath Tripathi** making my Japan stay pleasant.

I am very grateful to Kyushu Institute of Technology for making my stay in Japan pleasant and memorable. Particularly I would like to thank **Ms. Yasuko Nagamatsu** for kind support provided.

Moreover, I indebted to my parents **(Mr. Murugan V and Mrs. Vijaya M)**, my sister family **(Mrs. Suganthi and Mr. Lokeshnithin)**, and my grandparents (**Mr. Pachamuthu N and Rayammal P**).